Imperfections: using defects to program designer matter

Meeussen, A.S.

3. Topological defects produce exotic mechanics in complex metamaterials[1]

Abstract

We uncover the distinct mechanical signature of topological defects, introduced in chapter 2 via experiments and simulations, and leverage this to design complex metamaterials in which we can steer deformations and stresses towards different locations.

3.1. Introduction

Metamaterials' unusual mechanical properties arise from the geometry of their unit cells[7–10,15–22]. Many strategies exist to create metamaterials, on a spectrum of formality: from traditional and intuitive design[46] to computerized machine-learning strategies[47], topology optimization[48] and genetic algorithms[49]. While such automated techniques are valuable, a skilled operator is still needed to ensure that a suitable design can and will be found within a reasonable time. This is a classic bottleneck: reinventing the wheel (or a skyscraper) with modern techniques takes time and effort, and there are plenty of good design templates ready to go. In other words, innovative design is hard, and metamaterials are no exception.

There is therefore a need for conceptual work that helps formalize metamaterial design using simple, understandable design rules. Ideally, such design rules function as a guidebook, for example by prescribing how architectural elements should be combined to obtain desired stiffness or reconfigurability; or more indirectly, which mathematical rules the modelled system should obey[21,50]. Most seminal and ground-breaking work in this community has managed to do this by considering analogies between classical mechanics, and optical, acoustic or electronic systems[24,44,51].

In this chapter, we design metamaterials that harness mechanical frustration, analogously to geometric frustration in spin-ices. In the previous chapter, we discussed how to create stacked, compatible networks, and how to make these incompatible via local or topological defects. Evidently, defects frustrate the mechanical deformation of our metamaterials. We now explore the effect of these defects on the mechanical response of our metamaterials. We first present simple constitutive models and experimental realizations of in section 3.2. We then discuss the physical manifestations of (in)compatibility due to the presence of defects in section 3.3 and use this understanding to formulate a protocol to mechanically distinguish structural and topological defects. Finally, we harness the distinct mechanical response of topological defects to design localized deformation fields in larger networks in section 3.4. We discuss the impact of our work in section 3.5.

[1] The work presented in this chapter is based on Refs.[13] and [14].

3.2. Probing frustration: models and experiments

Studying the mechanics of our networks requires experiments and models. In this section, we discuss the construction of both.

Experimental realizations of our complex metamaterials are produced via selective laser sintering (section 3.2.1). In these experimental samples, stiff bars connected via soft living hinges (that is, thin and flexible filaments made of the same material as the bars) correspond to the bonds and nodes of the initial design. This design method produces macroscopic, malleable structures that can be actuated by hand. In order to gain a deeper understanding of our experimental results, we describe two minimal models that relate forces and displacements, which work on the network's connecting nodes, to elongations and tensions of its bonds. We first treat a mechanical model consisting of Hookean springs connected by freely hinging nodes (model FH, section 3.2.2), and then decorate this model with a torsional hinge stiffness (models TR and LTR, section 3.2.3), as illustrated schematically in Fig. 3.3a. We expect this latter model to correspond more closely to the actual behaviour of our experimental samples, whose living hinges have a finite stiffness. We compare the experimental and modelled sample's behaviours in section 3.2.4.

3.2.1. Experimental realizations

3D-printed versions of our complex mechanical metamaterials realize the network's bonds by thick elastic beams and its hinges by thin joints. We discuss their fabrication and probing strategy, as well as error estimates during deformation measurements, below.

Printing process

As illustrated in Fig. 3.1, experimental realizations of our complex metamaterials are produced using a Sinterit Lisa 3D printer with thermoplastic polyurethane powder Sinterit Flexa Black, processed at a sintering layer height of 0.1 mm at the "softer" setting[52,53]. The reported Young's modulus of the base material printed at these specifications is 4 ± 0.5 MPa, and the final printed networks have a height of 5 ± 0.2 mm. The individual bars of the network are realized as thick beams, connected by thin beams—functioning as living hinges—at each joining node, which is marked in contrasting white (Fig. 3.1a,b).

The final printed networks have a height of 5 ± 0.2 mm, a length of 107 ± 2 mm. Each bar has a length of 10 ± 0.2 mm, and the narrowest part of the connecting hinges has a length 0.5 ± 0.2 mm and width 0.7 ± 0.2 mm. An impression of the printed samples, including overall dimensions and sizes of the constituent parts, is shown in Fig. 3.1c-d.

Sample deformation measurements

To quantify the deformation of our experimental samples, we track the positions of their nodes. High-resolution images of the sample under various external probing conditions are obtained using a Canon EOS 750D camera, by placing the network on a horizontal surface at a constant position of approximately 30 mm from the camera body. The 6000-by-4000-pixel images are analysed using a custom program created using the Python 3

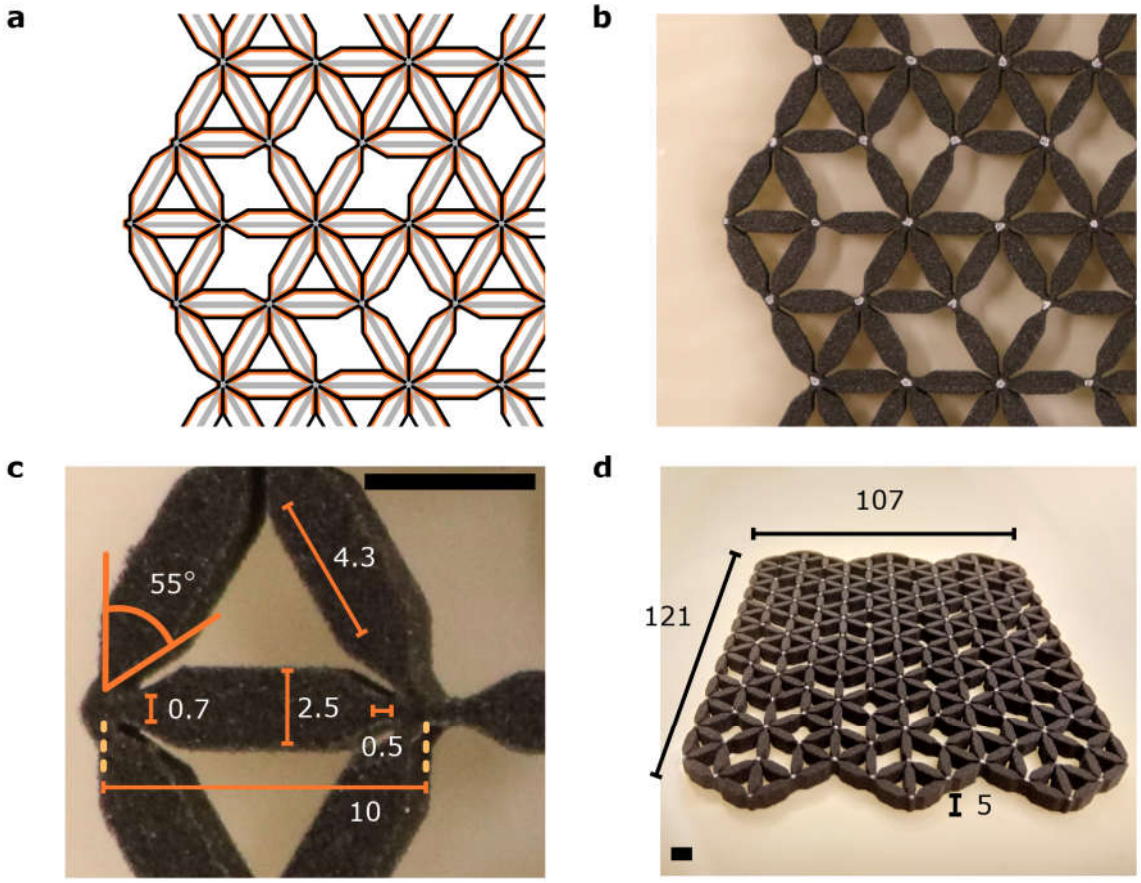

Fig. 3.1.: Fabrication of experimental samples. **a,** A section of the original network design is shown (grey lines). The network design is converted to an outline (black lines) suitable for fabrication with a Sinterit LISA 3D printer. The final printed sample has smaller dimensions (approximated by orange lines) due to resolution limitations. **b,** A section of the printed specimen, created by laser-sintering powdered thermoplastic polyurethane FlexaBlack, is shown. The network's bonds are realized as thick bars tapering to thin hinges that meet at a node. Nodes are manually marked with white dots after printing. Scale bar: 5mm. **c,** Dimensions of the sample's constituent parts are indicated in millimetres unless noted otherwise. An error of 0.2mm and 5° is estimated for lengths and angles respectively. **d,** A rectangular sample of 6 rows and 11 columns of building blocks and its overall dimensions in mm. Scale bar: 5mm.

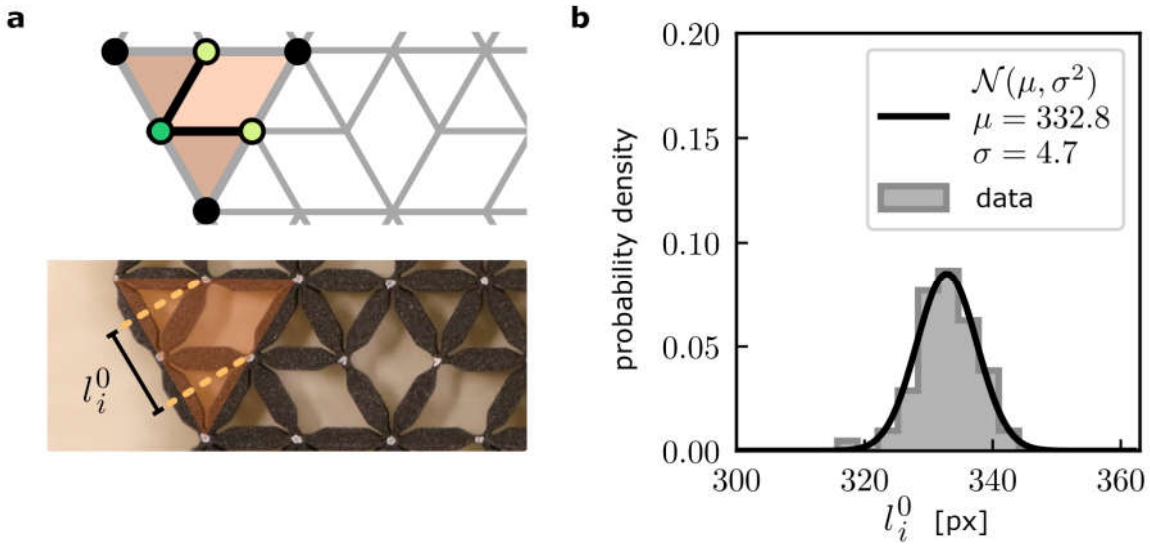

Fig. 3.2.: Deformation measurement error estimates. a) A section of a metamaterial design and its corresponded printed sample. The network's building blocks (one highlighted in orange) are characterized by a block rest length l_i^0, corresponding to the separation distance of the blocks' majority edge-nodes (top, light green circles). **b** The initial block rest lengths l_i^0 in the sample, measured in pixels by imaging and tracking the network's nodes, are normally distributed (grey area) with a mean μ and standard deviation σ (black line). Assuming the distribution's mean corresponds to the designed bar length of 10 mm, an imaging resolution of 33.3 px/mm and a standard deviation 0.15 mm on length measurements are obtained.

scripting language. Since the material's nodes are marked in a contrasting colour, the node positions of the network at rest and under various deformation conditions may be obtained from the images, and subsequently used to calculate node displacements and changes in node separation distance.

Error estimates

Length measurements in images of the samples are sensitive to errors, which we estimate as follows. Fig. 3.2a illustrates how initial block lengths l_i^0, or separation distance of each network block's majority edge-nodes, may be measured. Fig. 3.2b shows a typical distribution of initial block lengths l_i^0 in units of image pixels. The data shown were obtained for a representative sample of the size shown in Fig. 3.1d. The probability density estimate of initial block lengths is normal to good approximation, $\mathcal{N}(\mu, \sigma^2)$, with a mean $\mu = 332.8$ px and standard deviation $\sigma = 4.7$ px. We take the distribution's mean value to be equal to the designed node spacing of 10 mm to obtain an image resolution of 33 px/mm and a corresponding standard deviation $\Delta l = 0.15$mm, or approximately 5 image pixels. For simplicity, we assume that all errors are uncorrelated, which may lead to an underestimation of the measurement uncertainty.

3.2.2. Model FH: freely hinging spring network

To model the mechanical response of a complex network of stiff bonds and soft hinges, we may to treat its bonds as Hookean springs connected by freely hinging nodes. As

discussed by Pellegrino[54], the network's response to manipulation in the linear regime of small displacements can then be calculated straightforwardly. We describe the calculation method below, obtaining two sets of matrix equations that relate a network's nodal displacements and forces to its bond elongations and tensions.

In *model FH*, we capture the linear response of our systems based on networks of Hookean springs connected by freely hinging nodes[55], such that each bond contributes a potential stretching energy $\epsilon_s = \frac{k_s}{2}e^2$, where k_s is the bond's stiffness and e the elongation from its equilibrium length.

As shown in Fig. 3.3b, each node i supplies two degrees of freedom via spatial displacements $u_{x,i}$ and $u_{y,i}$, while a bond of length l^0 between two nodes at locations $\mathbf{r}_i$ and $\mathbf{r}_j$ constrains these motions by resisting linearized bond elongation $e_{ij} = \frac{\mathbf{r}_i - \mathbf{r}_j}{|\mathbf{r}_i - \mathbf{r}_j|} \cdot (\mathbf{u}_i - \mathbf{u}_j)$. For a large network, the vector of bond elongations $\mathbf{e} = (...e_{ij}...)$ is related to the vector of nodal displacements $\mathbf{u} = (...u_{x,i}, u_{y,i}...u_{x,j}, u_{y,j}...)$ via a compatibility matrix $\mathbf{R}$ so that $\mathbf{e} = \mathbf{R}\mathbf{u}$. Each row of $\mathbf{R}$ relates the displacements of two nodes to the elongation of their connecting bond. Bond elongations result in bond tensions τ_{ij}, which we will also refer to as *stresses*, via a constitutive equation: $\tau = \mathbf{K}\mathbf{e}$, where $\mathbf{K}$ is a diagonal matrix of bond stiffnesses that we set equal to the identity. Tensions are in turn converted to nodal loads $\boldsymbol{f} = (...f_i^x, f_i^y...f_j^x, f_j^y...)$ via $\mathbf{f} = \mathbf{R}^T\tau$. The collective displacements, elongations, tensions and forces fully characterize the network's mechanics.

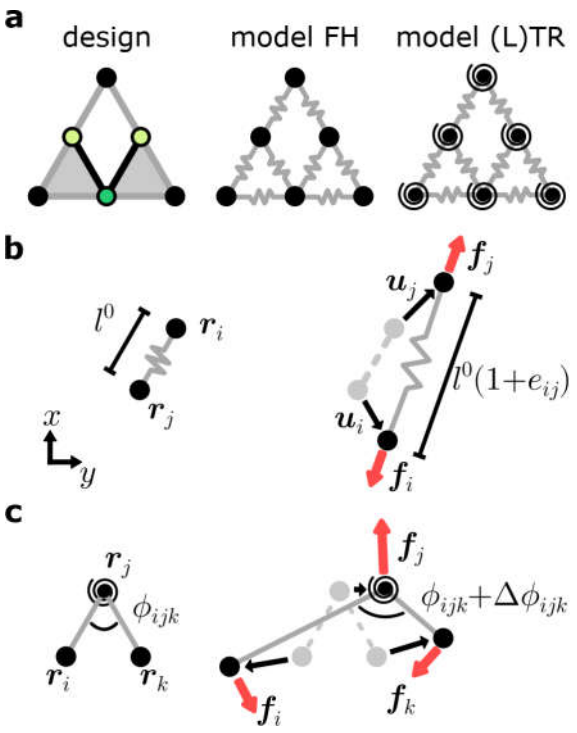

Fig. 3.3.: Modelling triangular building blocks. a, The building block design (left) corresponds to a network of freely hinging Hookean springs in model FH (middle) and is augmented with harmonic torsional hinges in models TR and LTR (right). **b,** Hookean spring mechanics. Left: two freely hinging nodes i, j, at initial positions $\boldsymbol{r}_i, \boldsymbol{r}_j$, and their connecting Hookean spring with rest length l^0 are shown in the x, y-plane. Right: the nodes undergo displacements $\boldsymbol{u}_i, \boldsymbol{u}_j$ as their degrees of freedom, elongating the spring by a dimensionless strain e_{ij} and producing a tension in the bond. The nodes undergo external loads $\boldsymbol{f}_i, \boldsymbol{f}_j$. **c,** Torsional hinge mechanics. Left: three nodes i, j, k and their connecting torsional hinge at node j with rest angle ϕ_{ijk} are shown. Right: displacing the nodes produces an angular strain $\Delta\phi_{ijk}$ and results in a torque on the hinge. The nodes undergo external loads $\boldsymbol{f}_i, \boldsymbol{f}_j, \boldsymbol{f}_k$ in response.

To actuate the network, we generally displace selected nodes by small amounts, while the remaining nodes are free to move. To calculate the resulting mechanical response, we use the following three-step approach. First, we calculate node forces $\mathbf{f}$ resulting from imposing an initial displacement $\mathbf{u} = \sum_i \mathbf{u}_i$, where $\mathbf{u}_i = (0...u_i^x, u_i^y, ...0)$ are desired individual node displacements. Second, we determine how the network relaxes

to mechanical equilibrium so that node forces vanish except along the forcing directions: an appropriate compensating force is obtained via $\mathbf{f}_p = \mathbf{f} - \mathbf{N}_p\mathbf{N}_p^T\mathbf{f}$, where $\mathbf{N}_p$ is the matrix with forcing directions $\hat{\mathbf{n}}_i = (0...n_i^x, n_i^y, ...0)$ as its columns. The corresponding relaxation displacement $\mathbf{u}_p$ is then calculated from the compensating force $\mathbf{f}_p$ and the reduced compatibility matrix $\mathbf{R}_p = \mathbf{R} - \mathbf{R}\mathbf{N}_p\mathbf{N}_p^T$. Lastly, the final displacement state of the network is given by $\mathbf{u}_{\text{full}} = \mathbf{u} + \mathbf{u}_p$, and the matching bond elongations, tensions and node forces can be obtained from this displacement state. The resulting network response, valid in the regime of small deformations, is compatible with both the imposed node displacement and the conditions of mechanical equilibrium.

Note that the compatibility matrix is not generally invertible. Therefore, calculating the network's response to imposed forces as above needs to be done via a well-defined procedure[54] using the singular value decomposition and pseudoinverse of $\mathbf{R}^T = \mathbf{U}\mathbf{D}\mathbf{W}^\mathbf{T}$. Here, $\mathbf{U}$ and $\mathbf{W}$ are orthonormal matrices with the respective left and right singular vectors of $\mathbf{R}^T$ as their columns,while $\mathbf{D}$ contains the singular values of $\mathbf{R}^T$ on the diagonal. Partitioning $\mathbf{U} = [\mathbf{U_r}\ \mathbf{U_{ZM}}]$ into the vectors spanning the column space and ZM of $\mathbf{R}^T$, and $\mathbf{W} = [\mathbf{W_r}\ \mathbf{W_{SS}}]$ into the vectors spanning the row space and SSS, and partitioning $\mathbf{D} = \left[\begin{smallmatrix} \mathbf{D_r} & \mathbb{0} \\ \mathbb{0} & \mathbb{0} \end{smallmatrix}\right]$ so that $\mathbf{D_r}$ is a square diagonal matrix of ordered (from big to small) nonzero singular values, we can write:

$$\begin{aligned} \boldsymbol{\tau} &= \mathbf{W_r}{\mathbf{D_r}}^{-1}{\mathbf{U_r}}^T\boldsymbol{f} \\ \boldsymbol{e} &= \mathbf{K}^{-1}\boldsymbol{\tau} \\ \boldsymbol{u} &= \mathbf{U_r}{\mathbf{D_r}}^{-1}{\mathbf{W_r}}^T + \mathbf{U_{ZM}}\boldsymbol{y} \end{aligned} \quad , \tag{3.1}$$

where the last term indicates that zero-energy node displacements—or floppy modes—that may be added freely to the displacement, proportional to the indeterminate vector $\boldsymbol{y}$. There are two additional constraints that need to be satisfied: first, we must ensure that the imposed load leads to a determinate response and so does not overlap with any ZM via the requirement ${\mathbf{U_{ZM}}}^T\boldsymbol{f} = \mathbf{0}$. In addition, the bond elongations must be compatible with the network's geometry, requiring ${\mathbf{W_{SS}}}^T\boldsymbol{e} = \mathbf{0}$. Together, once the compatibility and stiffness matrices $\mathbf{R}$ and $\mathbf{K}$ are known, the equations in Eq. 3.1 allow us to calculate the network's linear response under imposed forces.

3.2.3. Model TR and LTR: torsionally rigid hinges

In our experimental metamaterials, constituent beams act as Hookean springs with fair accuracy, but hinges do cost energy to deform. We capture this hinging cost in *model TR*, in which bonds are modelled by Hookean springs as in model FH, but an energy contribution $\epsilon_h = \frac{k_h}{2}\Delta\phi^2$ is added. Here, k_h is a torsional hinge rigidity and $\Delta\phi$ is the deviation of the angle between two neighbouring bonds from its equilibrium value. Hence, the total potential energy of a modelled network is $\epsilon = \sum_b \epsilon_s + \sum_\alpha \epsilon_h$, where the first sum runs over all bonds, and the second sum over all angles between neighbouring pairs of bonds. In this model, the dimensionless stiffness ratio $\tilde{k} = k_s(l^0)^2/k_h$ thus sets the relative resistance of bond stretching versus hinge opening.

To obtain a network's configuration under actuation, we use a standard simulated annealing algorithm, to minimize its total potential energy by probabilistically updating the spatial coordinates of a randomly chosen node at each step, with Metropolis dynamics

and a dimensionless pseudotemperature decreasing gradually to zero over $50 \cdot 10^6$ steps. Model TR and simulations were devised and executed by Erdal C. Oğuz.

Model TR allows us to simulate nonlinear displacements of the metamaterial's nodes, but is computationally costly. As a less intensive alternative, the linear response of a mechanical network of Hookean springs connected by harmonic torsional hinges, which we shall call *model LTR*, can be modelled analogously to model FH.

The additional torsional constraints are included as shown in Fig. 3.3c. In the metamaterial, we consider each clockwise-ordered triplet of nodes i, j, k at locations $\mathbf{r}_i, \mathbf{r}_j, \mathbf{r}_k$. Two bonds connect nodes i and k to central node j; a harmonic torsional spring at the central node resists changes in the initial rest angle. Each node i supplies two degrees of freedom via spatial displacements $u_{x,i}$ and $u_{y,i}$, while a torsional spring between the three nodes constrains these motions by resisting linearized rest angle deviation, or angular strain, $\Delta\phi_{ijk} = (\frac{\mathbf{r}_i - \mathbf{r}_j}{|\mathbf{r}_i - \mathbf{r}_j|^2} \times (\mathbf{u}_j - \mathbf{u}_i) + \frac{\mathbf{r}_k - \mathbf{r}_j}{|\mathbf{r}_k - \mathbf{r}_j|^2} \times (\mathbf{u}_j - \mathbf{u}_k)) \cdot \hat{\boldsymbol{z}}$ with a torsional hinge rigidity k_h. Angular changes thus result in torsional tensions τ_{ijk} via a constitutive equation $\tau_{ij} = k_h \Delta\phi_{ijk}$.

The compatibility matrix $\mathbf{R}$ of the network is then constructed as for model FH, described in section 3.2.2, but the matrix is augmented with an additional row for each torsional spring. Each extra row relates the displacements of a node triplet to the angular change between their two connecting bonds. Similarly, a suitable stiffness matrix $\mathbf{K}$ for the entire network is found as for model FH. We create a diagonal matrix $\mathbf{K} = \left[\begin{smallmatrix} \mathbb{1} & \mathbb{0} \\ \mathbb{0} & \mathbf{k_h/k_s} \end{smallmatrix}\right]$, where the first block of diagonal entries correspond to axial stiffnesses which we set to unity as before, and the second block of diagonal entries correspond to relative torsional stiffnesses k_h/k_s. The stiffness matrix thus encodes the relative importance of the bonds' axial stiffness and the hinges' torsional stiffness.

The compatibility and stiffness matrices govern the mechanical behaviour of the network. Analogously to the strategies outlined in section 3.2.2, we can then calculate the collective displacements, elongations and angular changes, (angular) tensions, and forces in the network.

3.2.4. Comparing experiments and models

The 3D-printing process described in section 3.2.1 produces soft networks that are easily manipulated. How well these samples mimic the idealized mechanics of our simple geometric networks depends, among other things, on how well the floppy mode of the initial design (see chapter 2) is mimicked. A simple assessment shows that our samples reproduce the designed floppy modes qualitatively well, as we discuss here.

Our initial compatible network design and its floppy mode are shown in Fig. 3.4a-c. We investigate how well the printed network (Fig. 3.4d) reproduces the floppy mode by compressing it uniaxially (Fig. 3.4d). In this compression experiment, the network is placed between two parallel rigid blocks on its left and right sides and subsequently compressed by 3 mm, starting from a lateral dimension of 121 ± 2mm. By inspection, Fig. 3.4e-f show that the designed floppy mode is mimicked with reasonable accuracy.

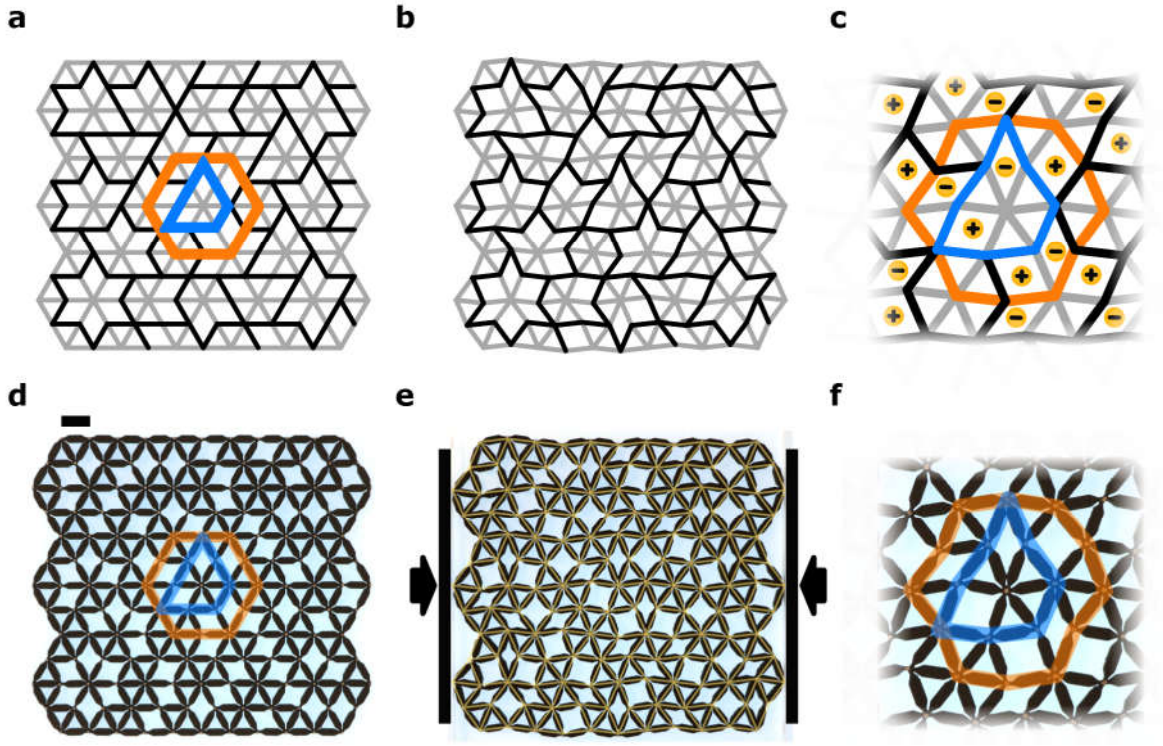

Fig. 3.4.: How printed samples deform compared to the designed floppy mode. **a,** An initial compatible network design is shown (edge and internal bonds shown as grey and black lines). A central hexagon (orange) and its even local loop (blue) are highlighted. **b,** The floppy mode of the network is visualized: this deformation mode does not change the length of any bonds. **c,** Zoom-in on the deformed central hexagon and its local loop. Positive and negative block spins corresponding to extension and contraction of the building blocks are indicated (yellow markers). **d,** Experimental realization of the design, 3D-printed as shown in Fig. 3.1. Scale bar: 10mm. **e,** The network is uniformly compressed by 3mm at its left and right edges (arrows). The network's designed floppy mode is superimposed (yellow lines). **f,** Zoom-in on the printed structure's central hexagon and local loop. Visual inspection shows a close match between the sample's deformation and the designed floppy mode.

The finite stiffness of the printed sample's hinges contributes to deviations from the designed floppy mode. This hinge stiffness, k_h, is included in models TR and LTR (see section 3.2.3), which crucially depend on the dimensionless *stiffness ratio*

$$\tilde{k} = k_s (l^0)^2 / k_h \ . \tag{3.2}$$

To accurately model our experimental findings, we estimate the order of magnitude of $\tilde{k}$ in our 3D printed networks by assuming all torsional and stretching deformations take place in the hinges, which have thickness t, length l, and width w and are made of a material with Poisson's ratio ν and Young's modulus E. To linear order, the bending and stretching stiffnesses of such a hinge are given by[56] $k_h = Et^3 w/[12(1-\nu^2)l]$ and $k_s = Etw/l$, resulting in a stiffness ratio $\tilde{k} = 12(1-\nu^2)l^{0\,2}/t^2$. Using the experimental values $l^0 = 10 \pm 0.2$ mm, $t = 0.7 \pm 0.2$ mm, and an experimentally estimated Poisson's ratio of $\nu = 0.43 \pm 0.03$ (see section 3.2.4 below), we estimate $\tilde{k} \approx 2000$ as our starting point. We refine this estimate later, in section 3.3.3, by matching the samples' experimentally measured and modelled properties directly.

Poisson ratio of flexible material

Experimental measurements of the FlexaBlack 3D-printed material's Poisson ratio were performed. The data were measured using an Instron 3336 series universal testing machine (UTM) managed with a Bluehill 2 software suite, outfitted with an Instron 2530-427 static load cell rated at 100N.

Three samples were printed according to the ISO-37 standard[57] for dumb-bell samples of type 1A. The gauge region of the samples was marked with contrasting white bars and measured to have a thickness 2.3 ± 0.05 mm, width $w = 5.3 \pm 0.05$ mm, and length $l = 20 \pm 0.3$ mm. Each sample was mounted in Instron 2710-series clamps and ensured to be at neutral load prior to testing. The sample was cycled four times from the neutral load position between -0.5 mm and 2.5 mm extension at a speed of 0.2 mm/s, while images of the sample at 3840 by 2748 pixels were recorded using a Basler acA3800 camera and lens of 75mm focal length. The camera was linked to the trigger output of the Instron UTM at a frequency of 1.33 Hz with custom-built recording software, to ensure that the recorded load data, extension data, and images were synchronized.

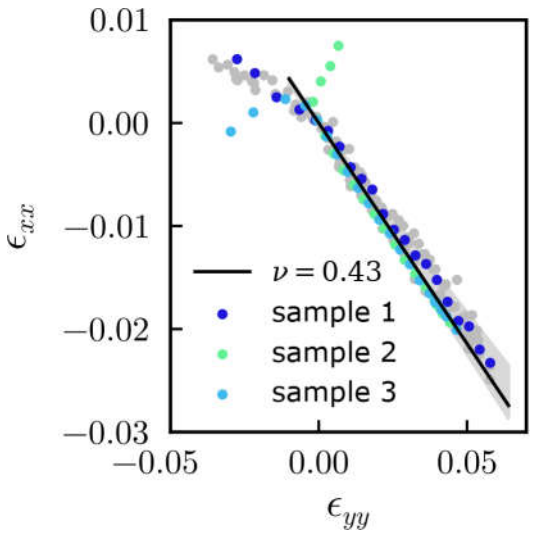

Fig. 3.5.: Poisson ratio of FlexaBlack 3D-printed material. Measurements of lateral and axial strain ϵ_{xx} and ϵ_{yy} of small samples of FlexaBlack material under a controlled extension applied by an Instron UTM. Three dumb-bell shaped samples compliant with ISO-37 type 1A (legend) were tested by extending and contracting them at least three times at a fixed speed; see text for details. The sample-averaged Poisson ratio $\nu = 0.43 \pm 0.03$ is indicated (black line). Additional measurements of sample 1 at lower and higher speeds were performed (grey circles). The minimal and maximal fitted Poisson ratios are indicated (grey area).

A custom Python program was used to extract the gauge section's length and width from the digital photographs using image thresholding. Data were averaged over the last three cycles. From these quantities, the engineering strain in lateral and axial directions were calculated via $\epsilon_{yy}(u) = l(u)/l(0)$, $\epsilon_{xx}(u) = w(u)/w(0)$ as a function of extension u. The measurement results are shown in Fig. 3.5.

An average Poisson ratio was obtained by fitting the relation between positive axial strain and lateral strain with a linear function for all three samples and averaging over the three measurements, as indicated in Fig. 3.5. The average Poisson ratio was found to be $\nu = 0.43 \pm 0.03$. Strain data for sample 1 were obtained additionally at testing speeds of $0.03, 0.02, 0.05, 0.1, 0.2$ and 0.5 mm/s and are indicated in grey in Fig. 3.5. The range of fitted Poisson ratios across all measurements are indicated by a light grey area.

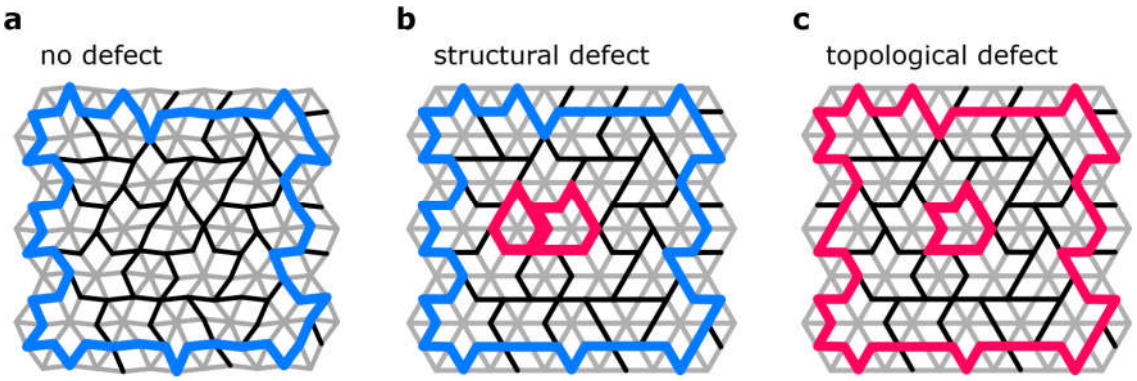

Fig. 3.6.: Networks with no defect, a structural defect, and a topological defect are structurally distinct. **a,** Compatible network design with no defect. Edge and internal bonds (grey and black lines) are shown. The network deforms according to its floppy mode as visualized. Internal bond loops around the system's boundary are of even length (blue lines). **b,** Frustrated network design with a structural defect, which blocks the floppy mode. Two local loops are of odd length (red lines). Loops around the system boundary remain of even length. **c,** Frustrated network design with a topological defect. One odd local loop is present. Loops around the system boundary are odd in length.

3.3. Mechanical signature of defects

We now turn our attention to the distinct mechanical response of metamaterials with structural, topological, or no defects. Our aim is to devise a mechanical measurement protocol that successfully distinguishes the presence of a defect as well as its character (structural or topological).

In chapter 2, we showed that the three network types have distinct architectures. There are two particular properties in which they differ. First of all, a compatible network has a system-spanning zero mode (Fig. 3.6a) that is absent in the presence of defects (Fig. 3.6b). Secondly, a topological defect is hallmarked by the fact that all loops around it contain an odd number of internal bonds, while loops around structural defects and compatible structures have an even perimeter (Fig. 3.6c). A testing protocol to distinguish the three network types should therefore measure the presence of a zero-energy deformation, as well as the parity of the loop of internal bonds running through blocks at the system's boundary.

We note that a mechanical implementation with infinitely rigid bars and perfectly flexible hinges has only zero and infinite energy deformations. This leads to a true floppy mode in the absence of defects, and a blocked system otherwise. In that case, structural and topological defects cannot be distinguished. However, once elastic deformations are allowed, such as in the experimental samples and models described in section 3.2, the mechanics becomes much richer and requires solving for mechanical equilibrium or performing direct measurements. It is precisely this mechanical richness that allows us to distinguish structural and topological defects.

In section 3.3.1, we introduce a testing protocol that uniquely distinguishes networks with a topological defect from those with no defect or a structural one, by merely probing the system's boundary. The results of this detection method are discussed in sections 3.3.2

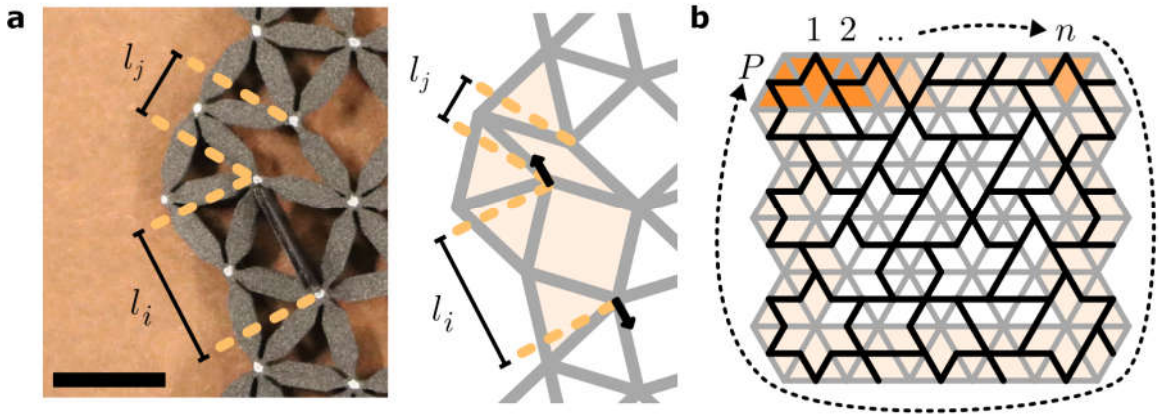

Fig. 3.7.: Probing the perimeter of a metamaterial. a, Left: a building block is extended experimentally by inserting a wedge, displacing its majority edge-nodes to a spacing l_i. The deformation of neighbouring block j is measured by the majority edge-node spacing l_j. Scale bar: 1 cm. Right: modelled extension is achieved by displacing the block's majority edge-nodes (arrows). **b,** For each pair of adjacent building blocks around the network's perimeter (dashed arrow), the extension of block j in response to the extension of block i is recorded consecutively. This results in pairwise measurements of block deformations l_i, l_j for all P block pairs $(1,2),...,(n,n+1),...,(P,1)$.

and 3.3.4, where we demonstrate that the unique bulk character of a network is identifiable in experimental samples as well as computational models via simple mechanical experiments. Our results show that there is a binary order parameter, or *topological probe*, measured at the system's edge, which is negative if and only if a topological defect is present. The two bulk material phases—with and without a topological defect—thus exhibit a unique bulk-boundary correspondence and are topologically distinct.

3.3.1. Detection protocol: measuring the boundary

Metamaterials with structural, topological, or no defects have distinct architectures and concomitant mechanical signatures. We detect (topological) defects in elastic metamaterials by considering pairs of building blocks at the system's boundary, deforming one building block and tracking the deformation of the other.

The basic idea is illustrated in 3.7a. Specifically, we extend a block i by forcing its majority nodes from a rest separation l^0 to a distance $l^0(1+\delta_i)$, measure the resulting deformation δ_j of neighbouring block j, and define a deformation *transfer factor*

$$q_{ij} = \delta_j/\delta_i \tag{3.3}$$

In a compatible metamaterial of freely hinging springs, $q_{ij} = \pm 1$, while incompatibilities or bending interactions cause $|q_{ij}| < 1$ due to elastic decay. Crucially, the sign of q_{ij} reflects the nature of the interactions between neighbouring blocks i and j, being antiferromagnetic (ferromagnetic) if $q_{ij} < 0$ ($q_{ij} > 0$). We separately measure the transfer factors between all neighbouring pairs of the P blocks around the network's perimeter;

define a *cumulative transfer product*

$$q_n := \prod_{i=1}^{n} q_{i,i+1} \tag{3.4}$$

that relates block 1 to block $n+1$; and introduce a normalized *topological probe*

$$Q := sign(q_P) \cdot |q_P|^{1/P} \tag{3.5}$$

that characterizes the full perimeter.

By definition, the magnitude and sign of the topological probe Q distinguish metamaterials with structural, topological, or no defects. In particular, the sign of Q precisely measures the parity of the closed loop of internal bonds around the boundary, being positive for a structural defect and negative for a topological defect. Note here that networks with an odd (even) number of odd local loops yield a negative (positive) Q. For a compatible system, deformations follow the global floppy mode, all building blocks deform with nearly equal magnitude and, since any loop around the system boundary is even, $Q \lessapprox 1$. An incompatible network has no global floppy mode, hence deformations decay more strongly away from the actuation point so that $|q_{ij}| < 1$ and $|Q| < 1$; crucially, the sign of Q should not be sensitive to this decay. A single structural and a single topological defect may thus be distinguished by the sign of Q, which gives the net topological charge enclosed by the system boundary.

3.3.2. Probing the entire boundary

We demonstrate the efficacy of our topological detection protocol in this section. We perform the detection protocol outlined above on three network designs, one compatible, one with a local defect, and one with a topological defect, using the design shown in Fig. 3.6a-c. The protocol is executed on experimental samples, as well as in models FH and (L)TR. An overview of the detection results is shown in Fig. 3.8, which figure we discuss below.

Fig. 3.8a indicates all edge blocks that are probed (orange triangles) from 1 to P. In the experimental samples, we actuate each edge block i by inserting a stiff wedge between its majority edge-nodes (recall Fig. 3.7a), separating them from an initial distance of 10 ± 0.2mm to 13.4 ± 0.2mm to obtain a block strain $\delta_i = 0.34 \pm 0.03$. In model TR, edge blocks are actuated by forcing their majority edge-nodes to separate to a block strain $\delta_i = 0.23$. A stiffness ratio $\tilde{k} = 3200$ is used to match experimental and modelled results (see section 3.3.3). For the topological detection scheme in the linear models FH and LTR, the results are independent of the imposed block strain to leading order. The node positions of the deformed sample in experiments as well as models are used to calculate the displacement of each node, after subtracting rigid-body translations and rotations. From this data we extract the initial and final lengths $l_{i,0}$ and l_i of the distances between the majority edge-nodes of each building block to determine the block strains $\delta_i = l_i/l_{i,0} - 1$. The resulting output block strains δ_j, transfer factors q_{ij}, cumulative transfer product q_n, and topological probe $Q(P)$ are calculated following Eqs. 3.3- 3.5.

Fig. 3.8b shows the cumulative transfer product, q_n, as a function of the number of

probed edge blocks n. Data are shown for networks with no defect (ND, top); a structural defect (SD, middle); and a topological defect (TD, bottom). Markers distinguish experimental and modelled results (legend). The numerical hinge model (L)TR and the experimental results show an overall excellent agreement, indicating that the behaviour of our networks is successfully captured by a simple network model of interconnected Hookean and torsional springs.

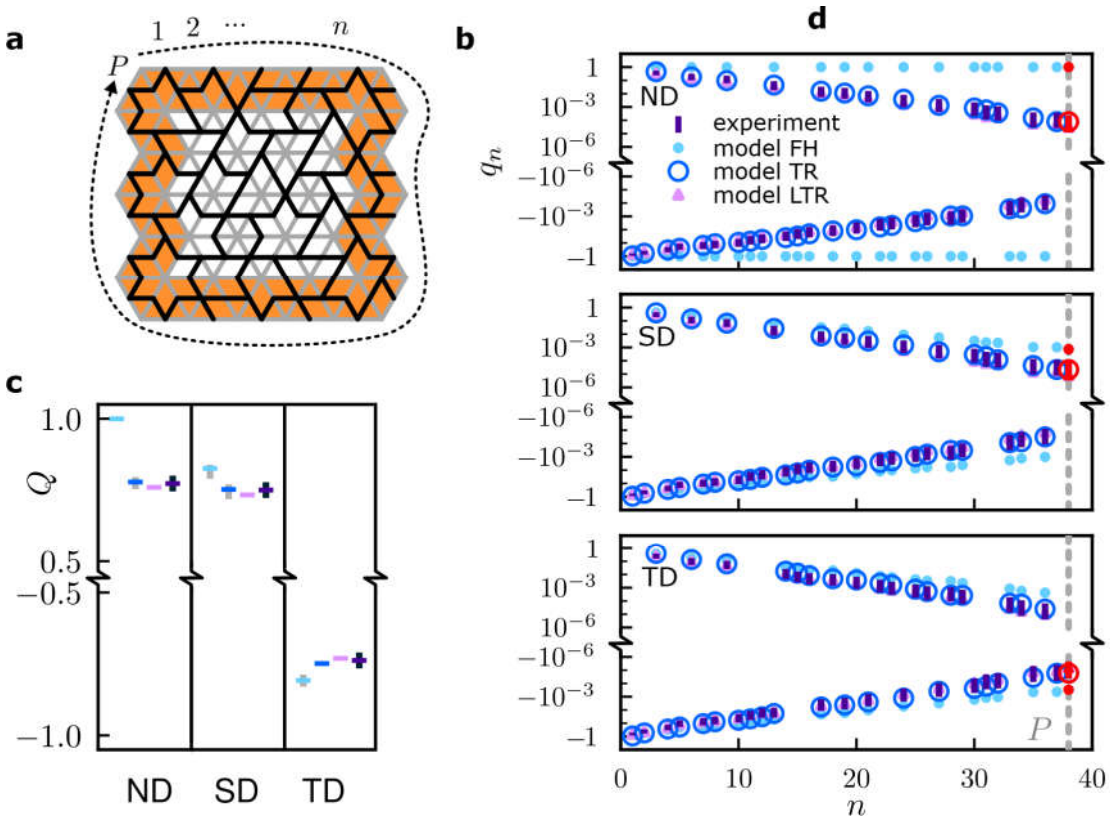

Fig. 3.8.: Defects are successfully distinguished by probing in a loop around the boundary. **a,** All boundary blocks (orange triangles) of a metamaterial are actuated consecutively (dashed arrow). With the protocol shown in Fig. 3.7, we track the response of each building block to actuation of its neighbour. **b,** The cumulative response of building block pairs around the system boundary is captured in the cumulative transfer factor q_n (Eq. 3.4). q_n is shown for structures with no defect (ND, top), a structural defect (SD, middle), and a topological defect (TD, bottom). Experimental and numerical data for identical network designs of each type are shown (legend). While the sign of q_n fluctuates rapidly in experiments, these trends are reproduced correctly in all models. The magnitude of q_n is successfully captured by models TR and LTR. The experimental data appear linear on a log-linear scale, implying an exponential decay of the deformation field across the material's building blocks under local actuation. **c,** The overall response of the network is summarized by the topological probe Q (Eq. 3.5), which is shown for the three network types (ND, SD, TD) in both experiments and models (legend). While the magnitude of Q depends on the details of each model, the sign of Q is negative if and only if a topological defect is present.

For all three network types, q_n shows an exponential decay with the exception of the compatible structure simulated with model FH. Recall that model FH corresponds to an idealized metamaterial in the small-displacement regime, consisting of Hookean springs connected by freely hinging nodes. For a system with no defect, deformations in model

FH thus follow the structure's global floppy mode, all building blocks deform with equal magnitude and, since any loop around the system boundary is even, $|q_n| = 1$. y contrast, since the experimental samples and model (L)TR have a nonzero hinge stiffness, they do not have a zero-energy floppy mode: even for a compatible network design, the sample's deformations decay away from the point of actuation. Thus, $|q_n| < 1$ due to elastic decay that stems from finite torsional resistance of the hinges[29]. Note that an incompatible network, which has either a structural or topological defect, has no global floppy mode. Hence, deformations decay away from the actuation point so that $|q_n| < 1$ for all incompatible structures, regardless of their experimental or modelled details.

Crucially, the sign of q_n is not sensitive to such details. The data show that the sign of q_n can vary wildly with $n < P$, reflecting the mixed antiferromagnetic and ferromagnetic interactions in our designs (see section 2.3.1). However, the sign of q_n at $n = P$ precisely measures the parity of the closed loop of internal bonds around the boundary, being positive for a structural defect and negative for a topological defect (Fig. 3.8b, red markers). A single structural and a single topological defect can thus be distinguished by the sign of q_P, which gives the net topological charge enclosed by the system boundary.

Finally, Fig. 3.8c shows the collected experimental and numerical results for the topological probe Q. The topological probes calculated for experimental samples and models (L)TR are similar in magnitude and smaller than unity, which results from their inclusion of a finite hinge stiffness. By comparison, the values of Q for model FH are consistently larger in magnitude. These results indicate that elastic decay—whether from a finite hinging stiffness or the presence of defects—blurs the distinction between defect-free metamaterials and those with a single structural defect, as both have $0 < Q < 1$. Nevertheless, our method allows us to unambiguously detect topological defects, for which the topological probe is exclusively negative: $Q < 0$.

3.3.3. Hinge stiffness: the right value

Here, we refine our estimate of section 3.2.4 for the stiffness ratio $\tilde{k} \approx 2000$, which describes the stiffness ratio between hinge bending and bond stretching. We compute the topological probe Q for model TR at various values of $\tilde{k}$ for networks corresponding to the experimental sample designs and compare the resulting values of Q to their experimental counterparts. Fig. 3.9 shows that the best match is found at $\tilde{k} \approx 3200$, of the same order of magnitude as the initial estimate, and the updated stiffness ratio is therefore used for model TR in all results presented in this chapter.

3.3.4. Probing a few boundary blocks

The detection scheme of section 3.3.2, while robust, requires a multitude of measurements proportional to the length of the material's perimeter. This becomes prohibitive for large systems. We now show that the topological character of a metamaterial can also be detected by considering a much smaller number of edge block pairs.

Specifically, we choose a subset of B roughly equally-spaced boundary blocks, actuating each block by extending it to a block deformation of δ_i, and calculate the transfer factor

$q_{ij} = \delta_j/\delta_i$ for each block pair. In analogy to the full cumulative transfer product q_n and topological probe Q, we define a diluted cumulative transfer product

$$q_n^B := \prod_{i,j}^{n} q_{ij} \ , \tag{3.6}$$

and a diluted topological probe

$$Q(B) = sign(q_P^B) \cdot |q_B^P|^{1/P} \ . \tag{3.7}$$

We calculate these diluted measures for networks of all three bulk types, using experiments and models. The resulting data are shown in Fig. 3.10.

First, Fig. 3.10a shows an example where $B = 7$ boundary building blocks (blue triangles) are probed.

The corresponding cumulative transfer product q_n^B is shown in Fig. 3.10b. Three sets of data, corresponding to $B = 38, 7,$ and $B = 4$ are shown (colours). Experiments and models are indicated with different markers (legend). The three network types are again represented: a material with no defect (ND, top), a structural defect (SD, middle), and one with a topological defect (TD, bottom) are indicated. Even though the data are more sparsely spaced when fewer building blocks are probed, the general trends of the cumulative product- fluctuations in sign as well as decay- reproduce well across all measurements. These findings again suggest an exponential decay of the deformation field across the material's building blocks under local actuation.

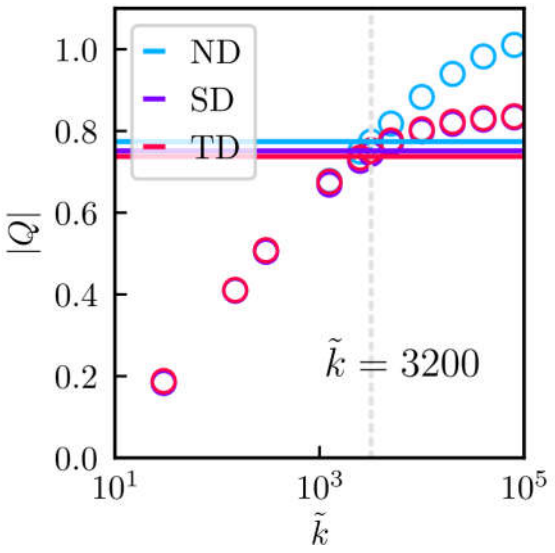

Fig. 3.9.: Comparing experiments and model TR, we select the right value for the modelled stiffness ratio $\tilde{k}$. The network response predicted by model TR yields a topological probe Q (see Eq. 3.5) that varies with the stiffness ratio $\tilde{k}$ between the bonds' axial stiffness and the nodes' hinging stiffness. Comparison of results from model TR (circles) and experiments (solid line) indicate that stiffness ratio $\tilde{k} \approx 3200$ (dashed line) yields the best match between experiment and model for networks with no defect (ND), and a good match for networks with a structural (SD) or topological (TD) defect.

Finally, in Fig. 3.10c, we show the diluted topological probe $Q(B)$ as a function of the fraction of boundary blocks that are probed, B/P. We find that the diluted topological probe $Q(B)$ has a sign that is independent, and a magnitude that is nearly independent, of the number of probed edge blocks, demonstrating the effectiveness of the diluted detection scheme for both experimental and model data. Hence, topological defects can practically and effectively be detected by probing a small fraction of the metamaterial's edge.

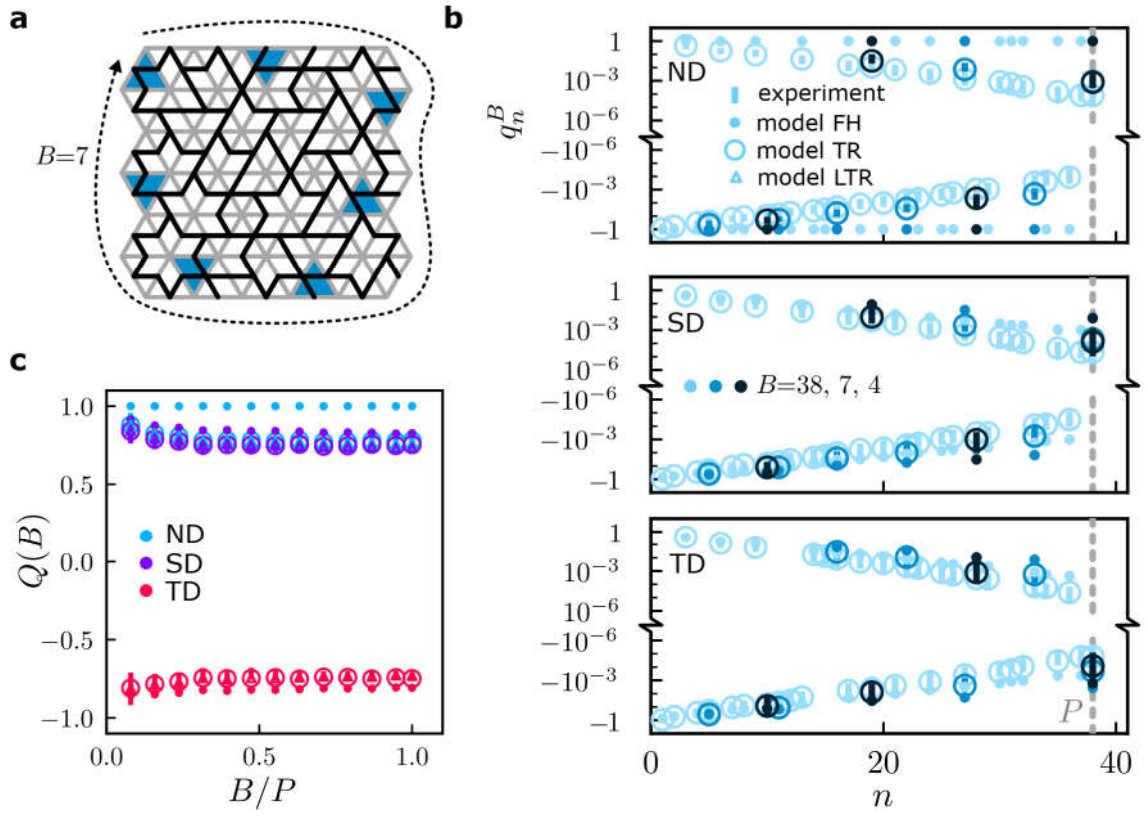

Fig. 3.10.: Defects are successfully distinguished, even with only a few measurements. a, B out of all P boundary blocks (blue triangles) of a metamaterial are actuated consecutively (dashed arrow). **b,** The cumulative response of building block pairs around the system boundary is captured by the diluted cumulative transfer factor q_n^B (Eq. 3.6). Structures with no defect (ND, top), a structural defect (SD, middle), and a topological defect (TD, bottom) were measured. Experimental and numerical data for identical network designs of each type are shown for various numbers of edge blocks B (legends). Experimental and modelled data show good agreement. The overlapping data for different values of B imply an exponential decay of the materials' deformation fields away from the probing point. **c,** The overall response of the network is summarized by the topological probe $Q(B)$ (Eq. 3.7), shown for the three network types (colours) in both experiments and models (legend). While the magnitude of Q depends weakly on the details of each model as well as the fraction of probed edge blocks B/P, the sign of Q is negative if and only if a topological defect is present.

3.3.5. Decay limits detection

The results in sections 3.3.2 and 3.3.4 show that the bulk character of a metamaterial can be detected robustly by probing the material's boundary. However, the detection results are affected by elastic decay.

Here, we explore how such decay influences the detection of defects. We show that the detection protocol is robust, as long as the elastic decay length for material deformations is larger than the spacing between the probed boundary blocks. The decay length is influenced by the stiffness ratio between hinge bending and bar stretching, as well as system size; however, the decay length stays above the unit cell spacing at all system sizes and at most stiffness ratios. These findings indicate that our detection protocol is robust across a broad range of metamaterial designs.

First, we note that the deformation field inside our metamaterials under local actuation appears to decay exponentially along the boundary. This finding is supported by the (diluted) cumulative transfer factors shown in Figs. 3.8b and 3.10b. There, q_n shows the ratio of block deformations away from the actuation point as a function of n, which corresponds roughly to the decay of material deformations as a function of distance. Using block strain as a measure of deformation, this means that a building block j at a distance d_{ij} from an actuated block i undergoes a block strain $\delta_j \approx \delta_i e^{-d_{ij}/d_Q}$, where δ_i is the strain on the actuated block and d_Q is the elastic decay length in units of the metamaterial's bond lengths, l^0. With this assumption for exponential decay, we find the following expression that relates the topological probe Q to the decay length:

$$d_Q \approx -\ln |Q|^{-1} \tag{3.8}$$

To check this expression, we note that the diluted topological probe $Q(B)^P \approx \pm e^{-\langle d_{ij}\rangle/d_Q}$ should decay exponentially with increasing average spacing between the probing points, $\langle d_{ij}\rangle$. Fig. 3.11a shows $Q(B)^P$ calculated for various values of the average block spacing $\langle d_{ij}\rangle$, the average distance between the geometric centres of consecutively actuated building blocks. Data shown were obtained for the three network types of Fig. 3.6 from experiments, model FH, and models (L)TR. The exponential relation $\pm e^{-\langle d_{ij}\rangle/d_Q}$ is overlaid on top of the measured data. The data suggest that d_Q is constant to fair approximation, supporting our assumption for exponential decay.

The exponential decay length d_Q is affected by two parameters: the stiffness ratio $\tilde{k}$ and the system size, which we explore now.

Fig. 3.11b shows the decay length d_Q as a function of the stiffness ratio $\tilde{k}$, where increasing $\tilde{k}$ corresponds to softer hinges and stiffer bars. The data shown were modelled using models TR and LTR for the three network types of Fig. 3.6. The data show three notable features. First, as $\tilde{k}$ increases and the hinges become softer, the decay length d_Q diverges in the absence of defects and saturates to a constant value when a defect (structural or topological) is present. The divergence of d_Q is due to the non-decaying floppy mode of compatible metamaterials with freely-hinging nodes, while the saturation of d_Q reflects a base level of geometric frustration in the presence of a defect. Secondly, there is a crossover stiffness ratio around $\tilde{k} \approx 1000$ at which the decay lengths for all three material types reach the same value. At this point, compatible and incompatible materials can no longer be distinguished by probing the boundary. This yields a practical

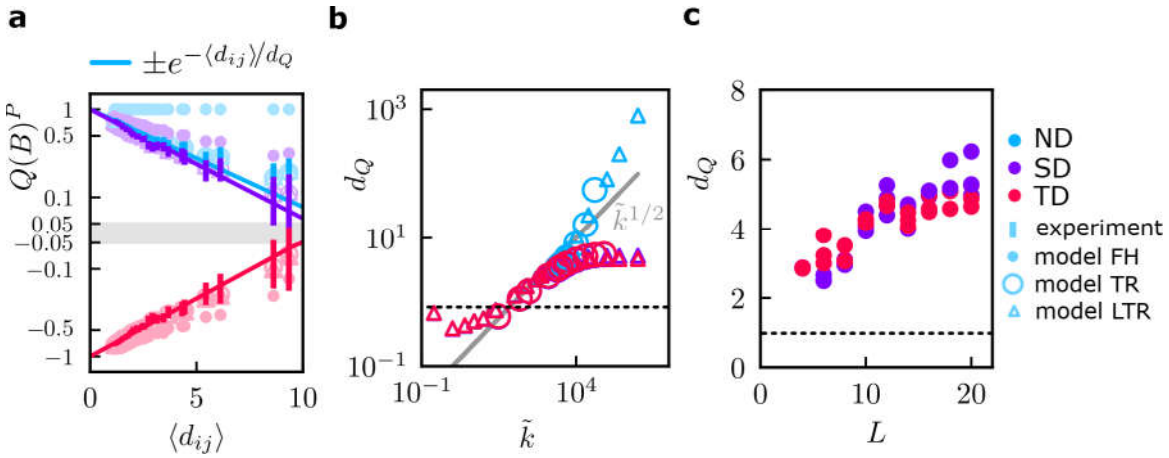

Fig. 3.11.: Elastic decay due to hinge stiffness and system size affects the topological probe Q. a, $Q(B)^P$ as a function of average block spacing $\langle d_{ij}\rangle$ for experiments, model FH, and model (L)TR (legend). The exponential trend $e^{-\langle d_{ij}\rangle/d_Q}$ confirms that d_Q (Eq. 3.8) is a fair measure of the elastic decay length of deformations around an actuated block. Data for one networks of each bulk type (ND, no defect; SD, structural defect; and TD, topological defect) are shown. **b,** Decay length d_Q varies with $\tilde{k}$, the stiffness ratio between spring and hinging stiffness. A low hinge stiffness, when $\tilde{k}$ is large, d_Q diverges for in the absence of defects: compatible and incompatible networks are easier to distinguish there. $\tilde{k}^{1/2}$ shown for reference[29]. **c,** d_Q increases with system size L. Results are shown for model FH, where $\tilde{k} \to \infty$.

rule of thumb for metamaterial design where defects should play a significant mechanical role: the stiffness ratio must then be larger than 1000. In our experimental samples, this corresponds to a maximal hinge thickness of approximately 1 mm (see section 3.2.4). Lastly, the decay length becomes smaller than the typical building block size, $d_Q < 1$, at a stiffness ratio of $\tilde{k} \approx 100$. At this point, the deformation field may decay so quickly that it is no longer possible to measure the deformation response of a building block when its neighbour is actuated. As a ballpark estimate, this crossover takes place in our experimental samples when the living hinges are made thicker than the connecting bars themselves. In that case, the three bulk architectures (with no defect, with a structural defect, and with a topological defect) cannot be distinguished from one another. In conclusion, for our defect detection protocol to be effective, the material's hinges must be sufficiently soft.

While the size of a metamaterials affects its decay length, the detection protocol works for both small and large networks. Fig. 3.11c shows d_Q as a function of network size L in units of bond length l^0, measured along the material's width. The data shown were modelled using model FH, with freely hinging nodes. The decay length shows a weak dependence on system size, increasing in magnitude for larger systems. The decay length does not dip below unity: $d_Q > 1$ for all system sizes. This suggests that our boundary detection protocol can distinguish metamaterial types regardless of size.

3.3.6. Error estimates

Using standard uncertainty propagation methods, we estimate the variance on quantities derived from the experimentally measured lengths l_i (see section 3.2.1 for an estimate of

the standard error Δl). These quantities are the transfer factor q_{ij}, cumulative transfer product q_n, and topological probe Q, defined as follows:

$$\begin{aligned} q_{ij} &= \frac{\delta_j}{\delta_i} = \frac{l_j/l_j^0 - 1}{l_i/l_i^0 - 1} \\ q_n &= \prod_{ij}^{n} q_{ij} \\ Q &= q_P^{1/P} \ . \end{aligned} \tag{3.9}$$

The following variance estimates are calculated for these quantities:

$$\begin{aligned} \Delta q_{ij}^2 &\approx \Delta l^2 q_{ij}^2 A_{ij} \ , \text{ where } A_{ij} = \left(\frac{(l_j/l_j^0)^2 + 1}{(l_j - l_j^0)^2} + \frac{(l_i/l_i^0)^2 + 1}{(l_i - l_i^0)^2} \right) \\ \Delta \log(q_n)^2 &= \Delta l^2 \sum_{ij}^{n} A_{ij} \\ \Delta Q^2 &\approx Q^2 \frac{\Delta l^2}{n^2} \sum_{ij}^{n} A_{ij} \ . \end{aligned} \tag{3.10}$$

The above estimates are used to calculate standard errors for the experimental data presented in this chapter.

3.4. Exotic mechanics with topological defects

The identification of distinct topological mechanical phases in our network designs opens up new vistas for practical design rules for structures with desirable mechanical properties. We discuss such design rules here.

In the previous sections, we showed that metamaterials with and without topological defects have fundamentally distinct architectures. This difference manifests mechanically via *geometric frustration*: defects generate strain when the material is actuated. We now show that geometric frustration is, at its heart, governed by *path parity*. We argue that controlling path parity allows us to design where stresses and deformations localize inside our metamaterials.

In section 3.4.1, we explain our design strategy from the bottom up. We study a pair of building blocks connected by one or more paths of internal bonds, corresponding to smaller and larger metamaterials. Under actuation of the two building blocks, the structure may deform freely or store energy. We show that the connecting paths' parity controls how deformations and stress distribute throughout the material. Section 3.4.1 demonstrates how to use path parity to design metamaterials with a directed, localized stress and deformation response under simultaneous actuation of two building blocks. We show that the presence of a topological defect produces a characteristic antisymmetric mechanical response, while the response of topologically trivial networks is symmetric. Finally, in section 3.4.3, we present the *mode splitting* phenomenon that underlies the asymmetric response in the presence of topological defects.

3.4.1. Mechanics and path parity

Here, we investigate the mechanical response of our metamaterials by exploring the behaviour of a single building block; a strip of stacked building blocks; and finally, a full 2D stacked metamaterial design.

Recall that a single building block has a local floppy mode, which can be activated by displacing the block's majority edge-nodes (Fig. 3.12a). The block responds by contracting or expanding, depending on the sign of the imposed displacements. This motion does not elongate any of the bonds, and does not produce geometric frustration.

Multiple building blocks can be chained into a single, one-dimensional strip. Consider the strip shown in Fig. 3.12b, top: its two end blocks (yellow triangles) are connected together by a single path of internal bonds (blue line). Recalling Eq. 2.1 in section 2.3.1, the parity of the path is positive, which corresponds to a ferromagnetic interaction between the two end blocks. When both end blocks are forced to extend (Fig. 3.12b, bottom, yellow markers), they are forced into a ferromagnetic state: their block spins are identical. This forcing matches the positive path parity, and as a consequence, the strip's floppy mode is actuated. Conversely, the strip shown in Fig. 3.12c consists of two end blocks connected by a negative-parity path (red line). Extending one end block and contracting the other imposes antiferromagnetic block spins, matching the path's parity and activating the strip's floppy mode. All blocks deform harmoniously.

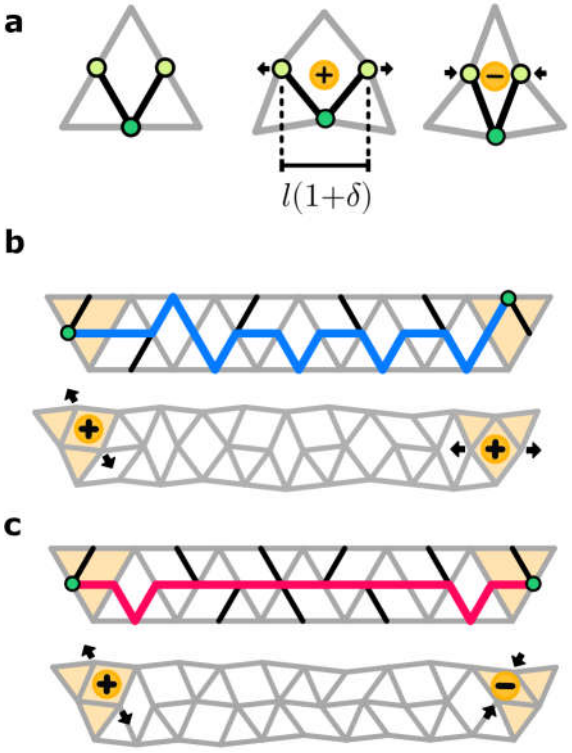

Fig. 3.12.: Understanding network mechanics with path parity. **a,** A single building block's floppy mode is actuated by displacing its majority edge-nodes (light green circles) to a positive or negative block spin (yellow markers), quantified by the block strain δ. **b,** How connected building blocks deform depends on the parity of their connecting path (section 2.3.1) Top: two blocks (yellow triangles) are connected by a ferromagnetic path (blue line). Bottom: the blocks' spins have the same sign (yellow markers) under actuation of the strip's floppy mode. **c,** Alternatively, two blocks are connected by an antiferromagnetic path (red line). The blocks' spins are opposite when the floppy mode is activated.

In other words: blocks are connected by paths. These paths have a positive or negative parity. If we impose block spins that match the paths' parity, the structure deforms easily. Equal block spins match positive paths, while opposite block spins match negative paths.

By contrast, imposing block spins that do not match the path parity produces geometric frustration, which we illustrate and quantify in Fig. 3.13. To ensure that we study geometric rather than elastic frustration due to finite hinge bending stiffness, we use model FH (see section 3.2.2) to simulate the network mechanics. In Fig. 3.13a, we

present a metamaterial strip of N_T building blocks, stacked along the x-direction in the plane. A path of positive parity connects the strip's end blocks. Enforcing opposite block spins by imposing a local block strain $\pm\delta_i$ (yellow markers) thus generates frustration, which manifests mechanically: first, building block deformations decay away from the actuated blocks, and second, bond lengths change. We measure changes in bond length using the bond strain δ_b (colours), and we measure block deformations using the block strain δ_j.

In Fig. 3.13b, we explore how bond and block strain are affected by the strip's length. We probe metamaterial strips of varying numbers of triangles N_T under incompatible forcing of magnitude $|\delta_i|$, and record the resulting bond and block strains δ_b and $|\delta_j|$ at a distance x along the strip's length. Note that all lengths have units of bond length l^0. In order to compare the results for various values of N_T, we divide the x-positions by the distance between the probed end blocks, $(N_T - 1)$.

At the top of Fig. 3.13b, we show the relative magnitude of output to input block strain, $|\delta_j|/|\delta_i|$, for each building block, sorted by normalized position. Block strains in the strip of Fig. 3.13a are indicated (black line), as well as results for various values of N_T (colours). The data collapses for all values of N_T. The block strains decay linearly to (near) zero in the middle of the strip: deformation of the building blocks is prohibited there. At the bottom of Fig. 3.13b, we show the bond strain $\delta_b(N_T - 1)/|\delta_i|$, normalized by the input block strain and the strip's total length. Here, too, the data collapses across strip lengths. Two features stand out: first, the bond strain is constant throughout the strip and shows no decay. Second, the bond strains take on discrete values, which we suggest to be a consequence of the six-fold symmetry of the bond's orientations.

The fact that block strains decay linearly while bond strains remain constant along the strip's length is reminiscent of Hookean elastic behaviour. Consider a piece of material with Young's modulus E, length L, and area A. The energy stored in this material when its length increases by ΔL is given by $\mathcal{E} = AE\Delta L^2/L$. Evidently, the stored energy scales inversely with the material's length. For comparison, Fig. 3.13c shows the elastic energy $\mathcal{E}$ stored in a metamaterial strip with an effective length $N_T - 1$ between its two actuated ends. The data are shown on a double logarithmic scale. Comparison between the data and a reciprocal scaling (black line, inset) shows that in our metamaterials, the stored energy scales inversely with length. Effectively, our metamaterial thus behaves like a regular, Hookean solid: work must be performed and energy is stored in the network when the strip is geometrically frustrated.

Parity helps us understand frustration in larger networks as well. Fig. 3.14 shows three different network architectures: with no defect, with a structural defect, and with a topological defect. We show that the localization of frustration in these networks, under actuation of a pair of building blocks, correlates with the parity of the block pair's connecting paths.

Fig. 3.14a shows a compatible, defect-free network. A pair of building blocks (yellow triangles) is connected by a large number of paths that run throughout the material. Since all closed paths in the system are of positive parity—a requirement for compatibility, recall section 2.3—all paths between the block pair have the same parity. In this example, all paths are positive (e.g. blue lines). Actuating the blocks by extending

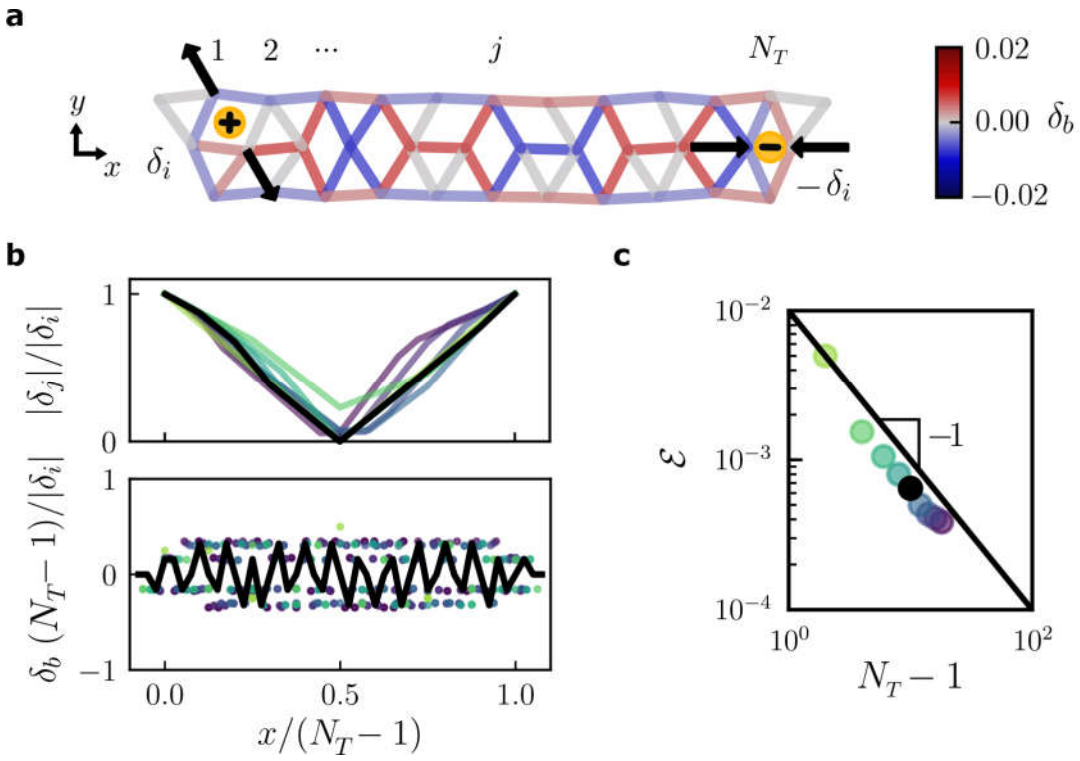

Fig. 3.13.: Geometric frustration manifests mechanically. **a,** Two building blocks connected by a ferromagnetic path of N_T building blocks (Fig. 3.12b) are given opposite block spins $\pm\delta_i$ (yellow markers) by displacing their majority edge-nodes (black arrows). Geometric frustration leads to energy being stored in deformed bars, producing a bond strain δ_b (colours). **b,** Blocks deform and bonds are strained under incompatible forcing. Normalized block strain (top) and bond strain (bottom) are shown as a function of normalized position $x/(N_T-1)$ along the strip. Colours correspond to strips of varying size N_T; black lines correspond to the structure shown in **a**. Top: relative block strain magnitude $|\delta_j|/|\delta_i|$ of the j-th building block. Frustration leads to a linear decay of block strain magnitudes. Bottom: local bond strain δ_b, normalized by the structure's length N_T-1 and input block strain δ_i, does not decay along the strip. Discrete bond strain values arise from the triangular architecture. **c,** Total elastic energy $\mathcal{E}$ stored in a strip as a function of its length N_T-1 under equal values of δ_i. $\mathcal{E}$ is inversely proportional to length (black line), consistent with normal elasticity (see text).

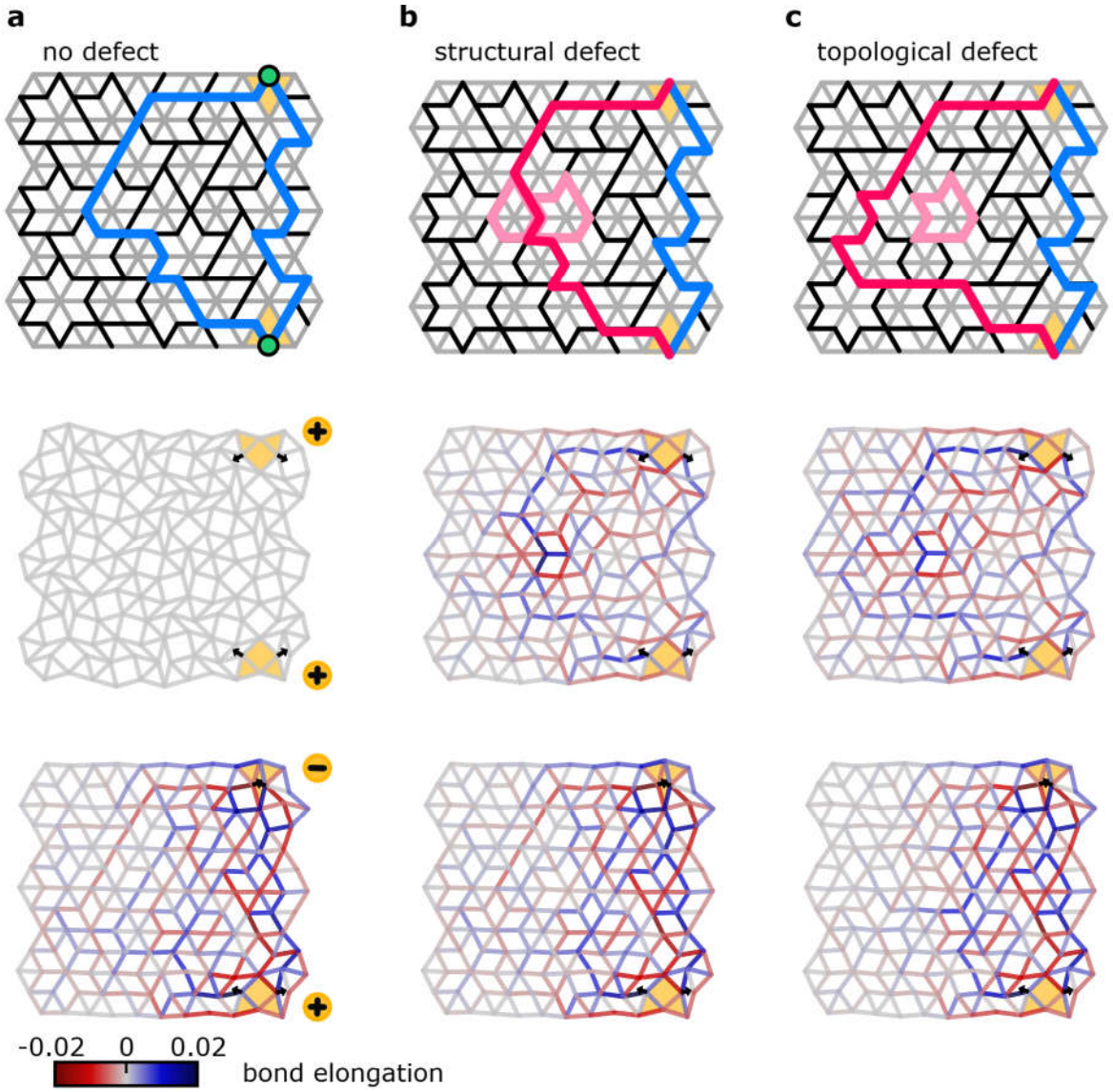

Fig. 3.14.: Path parity predicts frustration. a, Defect-free network (top) under compatible (middle) and incompatible forcing (bottom). Top: ferromagnetic paths (blue lines, e.g.) connect the minority nodes (green circles) of two building blocks (yellow triangles). Middle: enforcing compatible, ferromagnetic block spins (yellow markers, black arrows) activates the floppy mode. Bottom: enforcing antiferromagnetic block spins produces bond elongation along all ferromagnetic paths (colours). **b,** Top: a network with a structural defect (pink local loops) contains a single antiferromagnetic path (red line). Middle, bottom: ferromagnetic (antiferromagnetic) block spins produce bond elongation along the antiferromagnetic (ferromagnetic) path. **c,** Top: a network with a topological defect (pink local loop) contains both ferro- and antiferromagnetic paths that run along either side of the defect (blue and red lines, e.g.). Middle, bottom: ferromagnetic block spins produce geometric frustration along paths of antiferromagnetic parity, and vice versa.

them to the same block spin (3.14a, middle, yellow markers) thus matches the parity of all their connecting paths: there is no geometric frustration, and the structure deforms easily. Conversely, forcing the blocks to have opposite block spin (3.14a, bottom) is inconsistent with the parities of all their connecting paths. As a consequence, all paths are geometrically frustrated, and bonds throughout the system are elongated (colours). Since the density of frustrated paths is highest near the actuated blocks, bond elongations are larger there. In short: the mechanical response of a compatible network can be understood by considering the path parity between actuated blocks.

The mechanical response of a network with a structural defect may be understood in the same terms. When a structural defect is present in the network (Fig. 3.14b), most paths between our pair of building blocks (yellow triangles) have identical, positive parity (blue line, e.g.). However, any paths that run in between the two odd local loops that constitute the structural defect must have opposite, negative parity (Fig. 3.14b, red line, e.g.). As a result, when the building block pair is actuated to equal block spins, their deformation is consistent with the positive-parity paths and inconsistent with the negative-parity paths. The latter paths generate geometric frustration, and bonds along them will elongate. Since the density of negative-parity paths is highest at the structural defect, bonds in those areas experience the largest elongation (Fig. 3.14b, middle). Conversely, when the blocks are given opposite block spins, all positive-parity paths that go around the structural defect are frustrated and experience stress. Since no frustrated paths run between the defect's two odd local loops, bonds do not elongate much there (Fig. 3.14b, bottom). Evidently, frustration can be concentrated either inside or outside the area surrounding the structural defect, depending on the actuation parity.

Finally, the frustration situation changes once more for topological defects. Consider the network shown in Fig. 3.14c. Connecting paths running between our block pair (yellow triangles) have negative parity on the left side of the defect (e.g., red line), and positive on the right (blue line). This is a consequence of the fact that all closed paths in the system now have negative parity (see section 2.4). When the blocks are both dilated to a positive block spin (Fig. 3.14c, middle), all negative-parity paths are frustrated. Thus, the density of frustrated paths is largest on the left side of the system. Bond elongations are concentrated, correspondingly, on the left side of the topological defect. This situation is reversed when the blocks are forced to have unequal block spin (Fig. 3.14c, bottom): frustration is concentrated on the right side of the defect. In summary, in a network containing a topological defect, frustration may be concentrated on opposite sides of the defect under actuation of a pair of building blocks.

3.4.2. Stress and deformation steering

The previous section explores how the mechanical response of a network can be understood in terms of its connecting paths' parities. In particular, the mechanical responses of networks that have no defects, a structural defect, or a topological one have a very distinct spatial signature: frustration and deformation concentrate in different ways inside the networks' bulk. Here, we design metamaterials in which we exploit parity to steer deformations and stresses by actuating a small number of building blocks.

Consider a strip of metamaterial connecting two building blocks; depending on the con-

necting path's parity— positive or negative— extending both blocks respectively leads to a low energy deformation, or a highly frustrated response. Now define two pairs of blocks, i, j and i, j'. In the topologically trivial case, all paths connecting i and j have the same parity — and similarly for i and j'. Now consider a metamaterial with a centre hole, where the blocks are thus connected by two different strips (Fig. 3.15a). Designing i, j (i, j') to interact ferromagnetically (antiferromagnetically), expanding the former pair leads predominantly to deformations, while expanding the latter leads to a stressed, frustrated state. Fig. 3.15b shows the deformation and bond elongation fields for model FH, experiments, and model TR. In the experiments, two building blocks are simultaneously actuated by inserting wedges of 12.5 ± 0.2 mm width, inducing an majority edge-node separation from 10 ± 0.2 mm to 13.5 ± 0.4 mm. The modelled results were obtained by extending virtual building blocks to a strain of $\delta = \pm 0.35$. With these parameters, model TR matches experimental results with good accuracy: comparing the experimental and modelled deformation fields $\boldsymbol{u}_{\mathsf{exp}}$ and $\boldsymbol{u}_{\mathsf{TR}}$ via their cosine similarity $\hat{\boldsymbol{u}}_{\mathsf{exp}} \cdot \hat{\boldsymbol{u}}_{\mathsf{TR}}$, we find a match of 70 to 98 per cent. Fig. 3.15b shows that deformations and stresses (quantified by bond elongations) are distributed in the structures as expected.

In contrast, consider a non-trivial configuration with a topological defect in its excised centre, implying that the parities of the two strips are opposite (Fig. 3.15c). Expanding blocks i and j produces deformations in the positive-parity strip and stresses in the other, thus steering deformations and stresses to distinct parts of the sample; expanding blocks i and j' reverses the character of the upper and lower paths and the concomitant deformations and stresses (Fig. 3.15d). We note that actuating a single pair of blocks with the same or opposite parity (i.e., extending one and contracting the other) steers stresses and deformations similarly [13]. Crucially, actuating a *single* block simply leads to a smeared-out stress field, similar to what happens when an ordinary structural defect is present; only the combination of a topological defect and multi-site actuation leads to the stress steering shown in Fig. 3.15d.

With the above strategy, we actuate two distinct building block pairs inside a metamaterial to harness the antisymmetric signature of topological defects. A conceptually simpler method, which is experimentally slightly more complex but produces similar results, is achieved as follows. Consider a single block pair i, j. The two blocks may be actuated antiferromagnetically by expanding one and contracting the other, or ferromagnetically by expanding both. In the topologically trivial architecture shown in Fig. 3.15, a particular block pair i, j is connected by two positive-parity strips. Under ferromagnetic actuation, the entire structure deforms; under antiferromagnetic actuation, the structure is frustrated. Conversely, two blocks in the nontrivial metamaterial are connected by one ferromagnetic, positive-parity and one antiferromagnetic, negative-parity strip. Thus, (anti)ferromagnetic block actuation produces deformations in the (anti)ferromagnetic strip, and stresses in the other. We therefore observe a similar capacity for steering stress and deformation by actuating a single pair of building blocks in the metamaterial.

Hence, (excised) topological defects combined with targeted actuation at multiple sites allows for precisely designed, spatially steered mechanical responses.

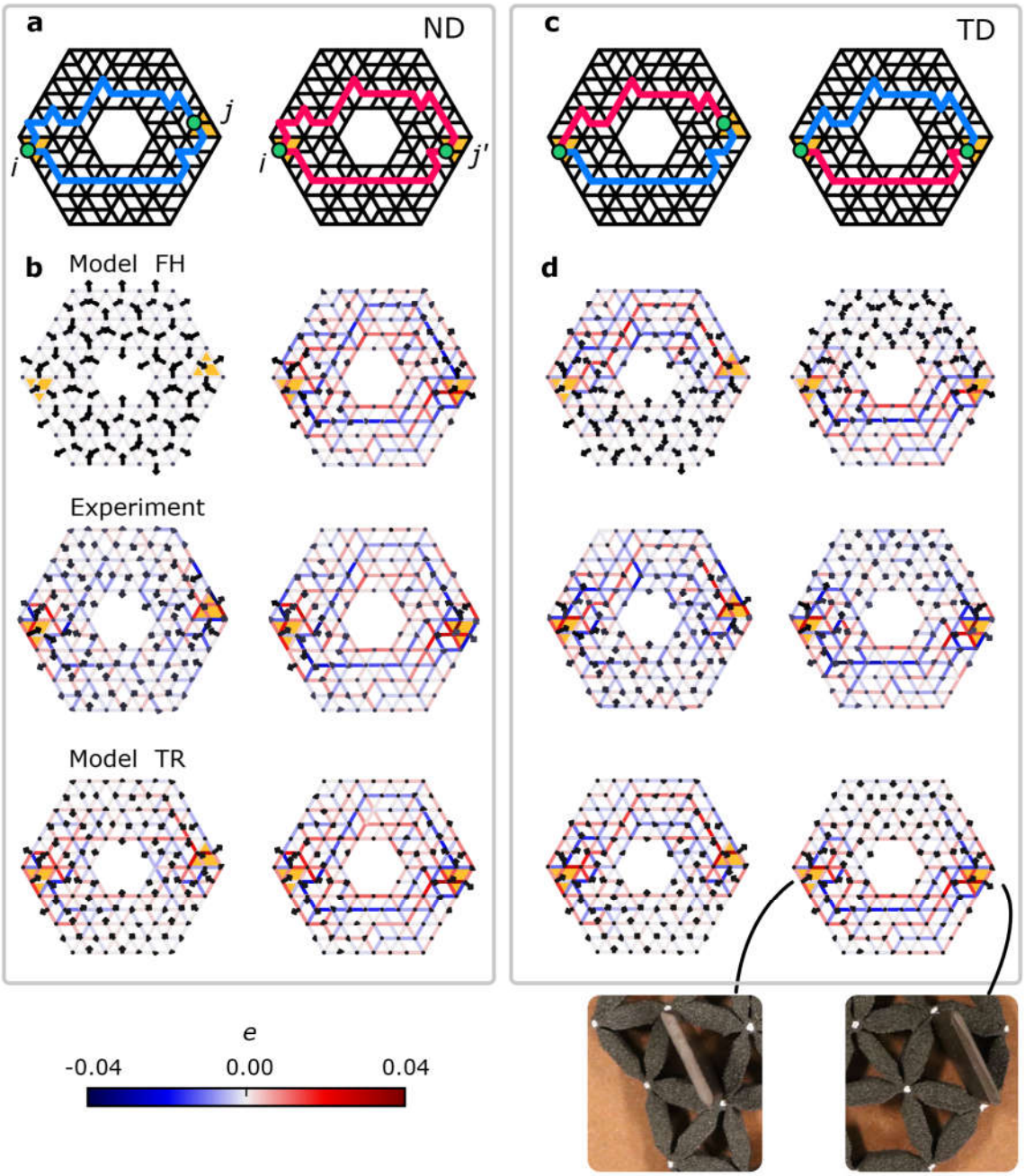

Fig. 3.15.: Stiffness steering. **a,** Compatible architecture (ND) with centre removed; blue and red indicate positive- and negative-parity paths between the actuation sites i, j and j' (yellow markers). **b,** Expanding blocks i and j mainly leads to displacements (left); arrows indicate deformation and are tripled in length for clarity, while bond colours indicate bond elongation e (colour bar). Expanding blocks i and j' mainly lead to bond stretching (right). **c,** Non-trivial architecture with a topological defect (TD) in the excised centre. **d,** Under simultaneous extension of the blocks i, j, bond stretching localizes in the upper portion of the sample, while node deformations localize in the lower part (middle); under actuation of blocks i, j', stretching localizes in the lower and deformations in the upper part (bottom). Stiffness steering is observed in modelled as well as experimental results, with model TR in quantitative agreement with experiments.

3.4.3. Mode splitting in the presence of topological defects

Topological defects produce unusual mechanics due to their architecture. Here, we explore the connection between architecture and mechanics from a different point of view: that of the structure's *normal modes*.

We first show that low-energy normal modes of a mechanical metamaterial, which are similar in nature to acoustic plane waves, dominate the structure's response to external probing. Secondly, we demonstrate that topologically trivial materials possess a single, symmetric, lowest-energy mode, which splits into two antisymmetric low-energy modes in the presence of topological defects. These antisymmetric modes underlie the exotic mechanics of topological defects.

Normal modes in metamaterials

We first consider the normal modes of a mechanical structure. Physically, normal modes are similar to stationary acoustic plane waves, where nodes are periodically displaced from their resting position across the metamaterial. Waves at higher spatial frequencies correspond to normal modes with proportionally larger energies.

In order to tease apart the effects of geometry and elasticity, we consider our metamaterials as freely hinging nodes connected by linear springs, as in model FH. In the linear regime of small displacements, normal modes of such a metamaterial are then configurations of node forces $\boldsymbol{f}_m$ that map to proportional node displacements $\boldsymbol{u}_m = c_m \boldsymbol{f}_m$.

To find a structure's normal modes, we use the following strategy. In section 3.2.2, node displacements and forces were shown to be related via a compatibility matrix $\mathbf{R}$, such that $\boldsymbol{f} = \mathbf{R}^T\mathbf{K}\mathbf{R}\boldsymbol{u}$. Here, $\mathbf{K}$ is a matrix of bond stiffnesses that we have set equal to unity. Mathematically, the normal modes are thus the right eigenvectors of the matrix $\mathbf{R}^T\mathbf{R}$. Since the transpose of the compatibility matrix can be written in terms of a unique singular value decomposition $\mathbf{R}^T = \mathbf{U}\mathbf{D}\mathbf{W}^T$, we may write $\mathbf{R}^T\mathbf{R} = \mathbf{U}\mathbf{D}\mathbf{D}\mathbf{U}^T$, where $\mathbf{U}$ and $\mathbf{W}$ are orthonormal matrices with the respective left and right singular vectors of $\mathbf{R}^T$ as their columns, while $\mathbf{D}$ contains the singular values of $\mathbf{R}^T$ on the diagonal. Thus, for each left singular vectors $\boldsymbol{u}_m$, there is a corresponding proportional force $\boldsymbol{f}_m = d_m^2 \boldsymbol{u}_m$. Therefore, the deformation vectors $\boldsymbol{u}_m$ are the normal modes of the system, with a corresponding eigenvalue d_m^2. The energy of such a mode, obtained by dotting $\hat{\boldsymbol{u}}_m$ with its resulting force, is $\mathcal{E}_m = \frac{1}{2} d_m^2$.

Note that each displacement field in the metamaterial can be written as a combination of normal modes: $\boldsymbol{u} = \sum_m (\boldsymbol{u} \cdot \hat{\boldsymbol{u}}_m)\hat{\boldsymbol{u}}_m = \sum_m c_m \hat{\boldsymbol{u}}_m$. The corresponding force is $\boldsymbol{f} = \sum_m d_m^2 c_m \hat{\boldsymbol{u}}_m$, resulting in an elastic energy $\frac{1}{2}\sum_m (d_m c_m)^2$. The magnitude of the force and energy scale quadratically with the singular values d_m.

We now consider the metamaterial's response under actuation of a single building block, and show that the resulting displacement field is a very particular linear combination of normal modes. The localized force needed to expand our building block can be written as a linear combination of load normal modes. This is reminiscent of a two-dimensional Dirac delta function around a point $\boldsymbol{r}_0$ (that is, a localized force), which can be expressed as a superposition of plane waves (or normal modes). We might expect the localized force

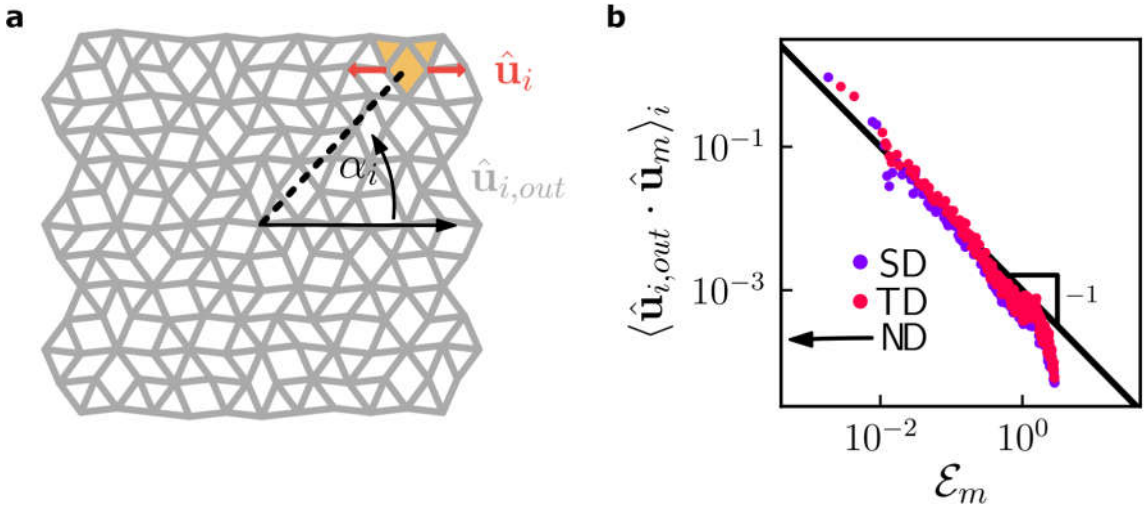

Fig. 3.16.: Displacement of a metamaterial under local probing in terms of normal modes. **a,** A metamaterial is actuated at a single boundary building block i (yellow triangle) at polar angle α_i with respect to the structure's centre. The input displacement field $\hat{\boldsymbol{u}}_i$ (red arrows) results in an output displacement field $\hat{\boldsymbol{u}}_{i,out}$ as shown. **b,** The relative contribution to $\hat{\boldsymbol{u}}_{i,out}$ of each of the structure's normal modes $\hat{\boldsymbol{u}}_m$ is plotted against the normal mode energy $\mathcal{E}_m$. Relative contributions are averaged over all building blocks i along the structure's boundary. Results for metamaterials with a structural (SD) and a topological defect (TD) are shown (colours). Metamaterials without a defect (ND) are dominated by a normal mode at $\mathcal{E}_m = 0$ (not shown). Displacement field contributions scale inversely proportional to the energy (black line).

to be a superposition of normal modes, in which the mode coefficients scale similarly to the coefficients of a Dirac delta function's discrete Fourier transform:

$$\delta(\boldsymbol{r} - \boldsymbol{r}_0) = \frac{1}{(2\pi)^2} \sum_{n=-\infty}^{\infty} \sum_{m=-\infty}^{\infty} e^{-in(x-x_0)\pi/L_x} e^{-im(y-y_0)\pi/L_y} \tag{3.11}$$

Evidently, the Dirac delta function's Fourier coefficients are equal to unity. Thus, we may expect the different load normal modes that make up our localized force to be represented at similar magnitudes: $\boldsymbol{f} \propto \sum_m \hat{\boldsymbol{f}}_m$. Mapping the load normal modes back to the displacement normal modes, we then hypothesize that the metamaterial's displacement field can be written as $\boldsymbol{u} \propto \sum_m 1/d_m^2 \hat{\boldsymbol{u}}_m$. Thus, under localized forcing, the displacement normal modes should be represented in the output deformation field with a magnitude that is inversely proportional to their corresponding energy $\mathcal{E}_m = \frac{1}{2} d_m^2$.

We confirm this hypothesis in our metamaterials as follows. Inside a metamaterial (Fig. 3.16a) we actuate each boundary building block i (yellow triangle, e.g.) at a polar angle α_i from the structure's centre. A displacement $\hat{\boldsymbol{u}}_i$ (red arrows) is imposed, and the resulting modelled deformation field $\hat{\boldsymbol{u}}_{i,out}$ is recorded. The relative contribution of each normal mode to the deformation field, $\hat{\boldsymbol{u}}_{i,out} \cdot \hat{\boldsymbol{u}}_m$, is identified. The relative contributions are then averaged over the material's boundary to reduce the impact of local architecture. Fig. 3.16b shows the resulting average contribution of each normal mode as a function of mode energy $\mathcal{E}_m$. The response of metamaterials with no defect (ND), a structural defect (SD), and a topological defect (TD) were investigated. Note that defect-free structures have a dominant floppy mode at $\mathcal{E}_m = 0$, which lies outside the domain of Fig. 3.16b. The data support that, to good approximation, each

normal mode is represented with a magnitude that is inversely proportional to its energy.

To summarize: under local actuation of a metamaterial, low-energy modes are strongly represented, while high-energy modes are not. Low-energy modes dominate the mechanical response.

Mode splitting

We now argue that the low-energy normal modes in metamaterials with and without a topological defect are fundamentally different.

Fig. 3.17a shows normal mode energy spectra for three metamaterials with distinct bulk characters: defect-free, with a structural defect, and with a topological defect. The first two structures are topologically trivial. They share a common feature: an energetic gap separates one low-energy mode from the rest. By contrast, the topologically nontrivial metamaterial exhibits two normal modes at low energy, separated by an energy gap from the remainder.

Fig. 3.17b illustrates the first two normal modes for each structure. The lowest-energy mode of the defect-free network (that is, the floppy mode) extends evenly throughout the network. In the presence of a structural defect, the lowest-energy mode is somewhat attenuated around the defect, but remains diffuse throughout the material. Conversely, networks with a topological defect have two low-energy normal modes (Fig. 3.17b, right), spatially localized to opposite sides of the system. These modes are *antisymmetric*: they cannot be combined to produce an evenly distributed deformation field. Any linear combination of the two modes results in a deformation field that is concentrated in one half of the system, in a phenomenon we call *mode splitting*.

Finally, we confirm that modes below the energetic gap dominate the mechanical response in our metamaterials. We calculate the deformation field $\hat{\boldsymbol{u}}_{i,out}$ in each structure, due to actuation of a single boundary building block at polar angle α_i (see Fig. 3.16a). Fig. 3.17c shows the overlap of each mode $\hat{\boldsymbol{u}}_m$ with the deformation field as a function of α_i. The data show that the lowest-energy modes (one for topologically trivial structures, and two for the nontrivial material) are represented at a much larger magnitude than higher-energy modes. In addition, the two antisymmetric normal modes in the presence of a topological defect dominate at opposite sides of the system (Fig. 3.17c, right).

As an aside, mode splitting gives rise to an interesting effect: when a topological metamaterial is periodically driven by squeezing and expanding two building blocks out-of-phase, the structure can support a polar wave that travels around the system. Conversely, topologically trivial structures can only exhibit planar waves that travel back and forth between the actuation points.

In short: the behaviour of a topological metamaterial is governed by two antisymmetric low-energy modes. Their antisymmetry gives rise to the stress-steering behaviour shown in section 3.4.2: deformations cannot be distributed evenly, but must be concentrated in one half of the metamaterial. Choosing the right actuation points gives control over which half.

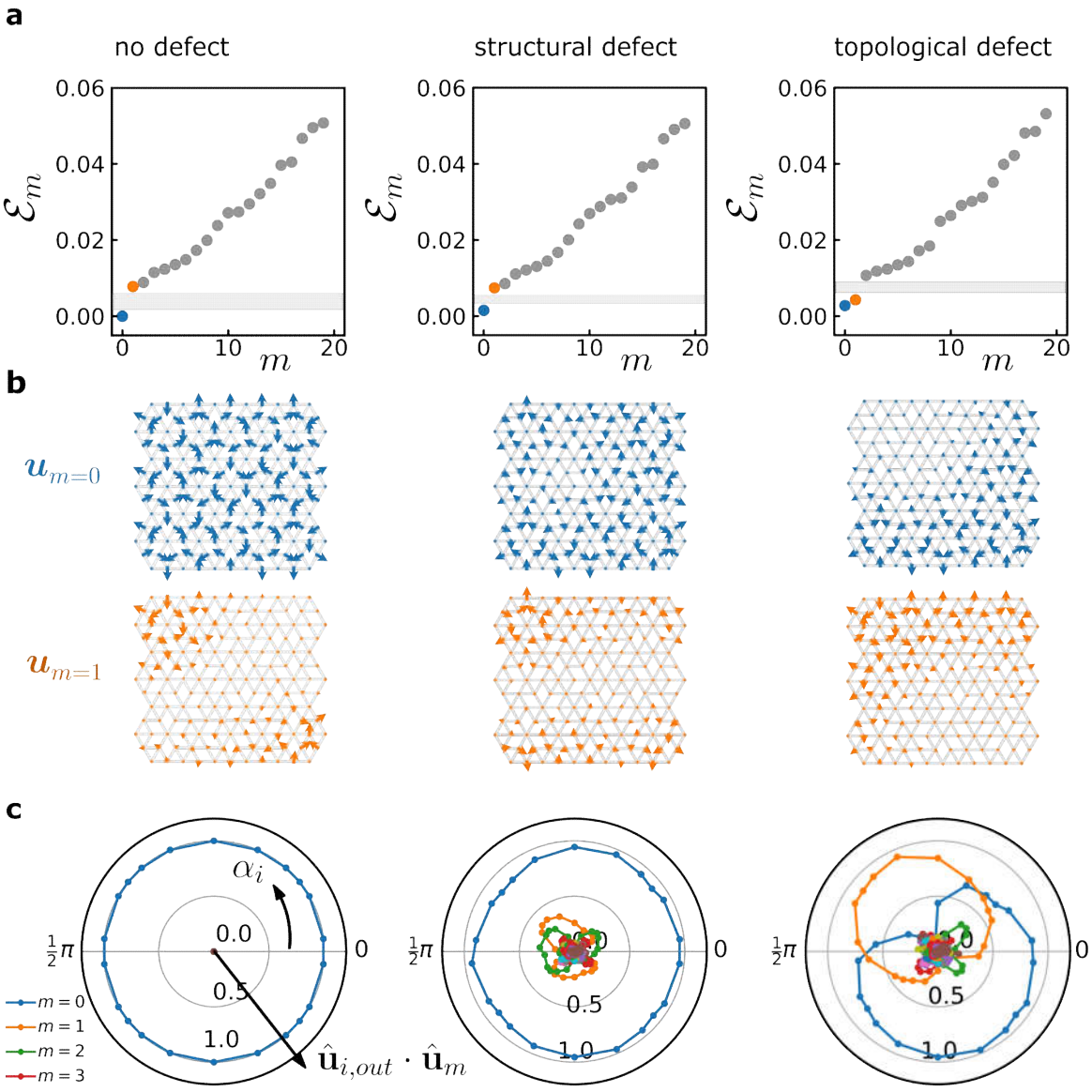

Fig. 3.17.: Topological defects produce antisymmetric normal modes. **a,** Energy spectrum $\mathcal{E}_m$ of the m-th normal mode of three representative metamaterials (no defect; structural defect; and topological defect) in model FH. Energy gaps are observed above the first or second mode (light grey areas). **b,** Displacement fields $\hat{\boldsymbol{u}}_m$ of to the two lowest-energy normal modes. Only structures with a topological defect exhibit two antisymmetric normal modes at similar energies. **c,** (A)symmetry of the materials' normal modes. Polar plots show the overlap of the normal modes (legend) with the structure's deformation field $\hat{\boldsymbol{u}}_{i,out}$, under extension of a single boundary block at polar angle α_i from the structure's centre (Fig. 3.16a). For structures without defects or with a structural defect (left, middle) the symmetric lowest-energy mode $m = 0$ (blue line) dominates the response. In the presence of a topological defect, the two antisymmetric modes $m = 0, 1$ contribute equally at opposite orientations (blue, orange lines).

3.5. Conclusions and outlook

In this chapter, we studied the mechanical response of the metamaterials introduced in chapter 2. We explored the mechanics of defects and determined that topological defects have a distinct signature that can be detected at the boundary of our metamaterials. We showed that this topological signature can be understood in terms of path parities between the metamaterials' building blocks, and harnessed this understanding to design metamaterials with characteristic symmetric and antisymmetric responses under two-point probing, showing how to use topological defects to steer stress and deformation fields inside our metamaterials. Finally, we argued that antisymmetric, low-energy mode splitting in the presence of topological defects underlies their stress-steering behaviour.

Previous work on mechanical metamaterials has been focused on studying compatible materials with one or several pre-programmed floppy modes[7,11,58,59]. However, designing the energy landscape of metamaterials at higher energies may help us create multifunctional materials that can perform more complex mechanical actions. Here, we have shown how topological defects may be used to engineer a directed finite-energy response. Our approach is based on an analogy to geometric frustration in spin-ices, which allows us to understand the mechanical response of metamaterials by considering interactions between different parts of the system via path parities. Our work thus presents an avenue into the design of metamaterial energy landscapes by harnessing controlled mechanical frustration.

This strategy to generate controlled and directed frustration may be extended to the design of novel classes of frustrated metamaterials, including origami, kirigami and 3D metamaterials[7,21,60], provided the deformations of the building blocks can be characterized by discrete, spin-like variables. The resulting complex metamaterials may impact future technologies concerning sensing, actuation, and soft robotics[61–63].

Acknowledgements

We thank Roni Ilan, Edan Lerner, Bela Mulder, Ben Pisanty, Eial Teomy and Ewold Verhagen for fruitful discussions, Jayson Paulose for co-developing code for the numerical model FH, and Dion Ursem for technical support. This research was supported in part by the Israel Science Foundation Grant No. 968/16.